

Structure and stability of magnetically confined mounds in a Neutron star

A Thesis

submitted to

Indian Institute of Science Education and Research Pune
in partial fulfillment of the requirements for the
BS-MS Dual Degree Programme

by

Anwasha Maharana



Indian Institute of Science Education and Research Pune
Dr. Homi Bhabha Road,
Pashan, Pune 411008, INDIA.

April, 2020

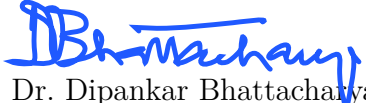
Supervisor: **Dr. Dipankar Bhattacharya**
Inter-University Centre for Astronomy and Astrophysics (IUCAA), Pune

© Anwasha Maharana 2020

All rights reserved

Certificate

This is to certify that this dissertation entitled *Structure and stability of magnetically confined mounds in a Neutron star* towards the partial fulfilment of the BS-MS dual degree programme at the Indian Institute of Science Education and Research, Pune represents study/work carried out by Anvesha Maharana at Inter-University Centre for Astronomy and Astrophysics (IUCAA), Pune under the supervision of Dr. Dipankar Bhattacharya, Distinguished Professor and Dean, Core Academic Programmes, IUCAA, Pune, during the academic year 2019-2020.



Dr. Dipankar Bhattacharya
(Thesis Supervisor)



Anvesha Maharana

Committee:

Dr. Dipankar Bhattacharya

Dr. Prasad Subramanian

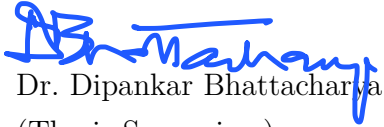
To Baba, for the challenge and belief

Declaration

I hereby declare that the matter embodied in the report entitled *Structure and stability of magnetically confined mounds in a Neutron star* are the results of the work carried out by me at the Inter-University Centre for Astronomy and Astrophysics (IUCAA), Pune under the supervision of Dr. Dipankar Bhattacharya and the same has not been submitted elsewhere for any other degree.



Anwesha Maharana



Dr. Dipankar Bhattacharya
(Thesis Supervisor)

Acknowledgments

I am grateful to my parents, Swarnaprava Maharana and Bijay Kumar Maharana for being brave and believing in my dreams, not just in academics but also for letting me navigate my decisions from an early age. I am immensely thankful to my uncle Antaryami Maharana(Baba), whose constant scepticism and challenge encouraged me to steer through difficult times during the Master's project.

On the academic side, I would like to thank Prof. Dipankar Bhattacharya for being kind and patient, guiding me to be creative and independent and showing me the way out of any mistake with a genuine smile. I thank Dr Dipanjan Mukherjee for the discussions and his valuable suggestions for the work. My heartfelt gratitude to Dr Prasad Subrmanian for his constant support and guidance as the Expert member in my Thesis Advisory Committee. I owe my sincere gratitude to IISER Pune and IUCAA for the endless exposure and opportunities to grow in academic and non-academic pursuits. Last but not the least, my friends at IISER whose company filled all the bittersweet moments with fun and memories.

Abstract

A high-mass X-ray binary (HMXB) is a binary system of a compact object, neutron star or black hole and a companion high mass star. The compact object accretes from its companion and the system emits strongly in X-ray. The proposed thesis project deals with an HMXB with neutron star as the compact object. The infalling matter from the companion star is obstructed by the magnetosphere of the neutron star and is guided by the magnetic field lines leading up to the poles, forming an accretion column along the magnetic field. This accretion column deposits the matter on the neutron star surface as a result of which an accretion mound is formed at each magnetic pole of the strongly magnetized neutron star. The mound distorts the local magnetic field, the imprint of which can be observed via Cyclotron Resonance Scattering Features (CRSF) in the X-ray spectrum. The spreading of matter onto the neutron star surface from the magnetically confined accretion mound has so far been poorly understood. How much matter can be retained in the mound and column is decided by interchange instabilities - such as ballooning instability, fluting instability and Parker instability - as well as dissipative processes such as ohmic diffusion and magnetic reconnection. Numerical investigation of some of these processes are attempted in this thesis. The matter accumulated in the mound adds a quadrupole moment to the mass distribution of the star, which then leads to the generation of gravitational waves as the star spins. The amplitude of these waves will be determined by the amount of mass in the mound and its density distribution, both critically dependent on the instabilities and dissipative processes. So, we try to understand the structure and stability of the magnetically confined accretion mounds formed at the poles of neutron star.

Contents

Abstract	xi
1 Introduction	1
1.1 Neutron stars	1
1.2 Accretion in neutron stars	2
1.3 Field burial and evolution of neutron stars	5
1.4 Accretion structures on neutron stars	5
1.5 Previous work in modelling the mounds	7
1.6 Motivation for the thesis	7
2 Static equilibrium structure of accretion mound	9
2.1 Introduction	9
2.2 Finding equilibrium solution for accretion mound	9
2.3 Solving GS equation	15
2.4 Discussion	20
3 Stability analysis of accretion mounds in 2D	21
3.1 Introduction	21
3.2 Numerical setup using PLUTO	22
3.3 Problem set up in PLUTO	25
3.4 Checking the stability of equilibrium solution using PLUTO	27
3.5 Adding excess mass	35
4 Polytropic vs Paczyński	43
4.1 Comparison on the basis of threshold height	43
4.2 Comparison on the basis of mass	44
4.3 Adding zero mean density perturbation	45
4.4 Discussion	46
5 Magnetohydrodynamic instabilities in the accretion mound	47
5.1 Causes of instabilities	47
5.2 Discussion	51

6 Summary	53
6.1 Conclusions	53
6.2 Future Work	54
Appendix A Numerical setup to solve GS equation	59
A.1 Successive Over Relaxation	60
Appendix B Equilibrium and stability in plasma confinement	63
B.1 Energy Principle	64

List of Figures

1.1	Schematic diagram of accretion column and mound	6
2.1	Magnetic flux profile of accretion mound with degenerate non-relativistic Fermi gas	17
2.2	Comparison of magnetic flux and height profiles for a mound with non-relativistic degenerate Fermi EOS and Paczyński EOS	19
3.1	A computational domain inside the accretion mound in PLUTO	27
3.2	Error distribution in mound density at equilibrium	28
3.3	Energy profile of the computational domain in the accretion mound at equilibrium	30
3.4	Evolution of overdensity profile of a $Z_c = 45m$ mound upon introducing velocity perturbation	32
3.5	Energy profile of the computational domain in the accretion mound upon introducing velocity perturbation	33
3.6	Evolution of overdensity profile of a $Z_c = 45m$ mound upon introducing zero mean density perturbation	34
3.7	Acceleration profile in a density perturbed accretion mound	37
3.8	Difference in pressure gradient in the accretion mound along z and r direction	37
3.9	Pressure gradient upon introducing density perturbation	37
3.10	Evolution of overdensity profile of a $Z_c = 45m$ mound upon introducing excess mass	39
3.11	Evolution of overdensity profile of a $Z_c = 60m$ mound upon introducing excess mass	39
3.12	Evolution of magnetic energy in mounds of different heights and density perturbation strengths	41
3.13	Evolution of kinetic energy in mounds of different heights and density perturbation strengths	42
4.1	Comparison of confined mass in mounds of same height in Paczyński and Non-relativistic EOS.	44

5.1	Magnetic flux profile of an unstable mound	48
-----	--	----

List of Tables

2.1	Maximum mass and density values for different mound heights	18
3.1	List of numerical schemes chosen in PLUTO	25
3.2	Normalization factors for physical quantities used in PLUTO	26
3.3	Evolution of error in density in different regions of a mound with $Z_c = 60\text{m}$	29
3.4	Evolution of error in density due to zero mean velocity perturbation .	31
3.5	Evolution of error in density due to zero mean density perturbation .	35
3.6	Percentage of excess mass added to the mounds of different heights and density perturbation strength (η)	38
4.1	Evolution of error in density due to zero mean density perturbation in Paczyński mounds	46

Chapter 1

Introduction

1.1 Neutron stars

1.1.1 History

According to the theoretically proposed idea by Baade and Zwicky(1934) neutron stars are expected to be formed in supernova explosions [48]. Although Oppenheimer and Volkoff (1939) modelled the neutron star matter as an ideal gas of free neutrons, research in this field was not active until the discovery of radio pulsars in 1967 by Jocelyn Bell. Franco Pacini (1967)[36] and Thomas Gold (1969)[18] independently proposed that the pulsed radiation could be coming from a rotating neutron star which is pumping the energy into the supernova remnant. This theory was soon backed up by the discovery of Crab and Vela pulsars situated in supernova remnants.

Further theoretical research on properties of neutron stars was stimulated by the discovery of compact X-ray sources like Cen X-3 and Her X-1, which were conjectured to be accreting from their companions. Optical and X-ray observations of binary sources were used to measure the masses of neutron stars [41]. Discovery of binary pulsars was brilliantly speculated to be used for the testing of gravitational radiation that have now been detected directly.

1.1.2 Properties

Neutron stars are dense gravitationally bound objects supported by neutron degeneracy pressure and repulsive strong interaction, formed by the core-collapse of main sequence stars of mass $8 - 30M_{\odot}$ [43]. A typical neutron star has a mass $1.4M_{\odot}$ and a radius of around 10km. High density ($\sim 10^7 \text{ g/cm}^3$) at the interiors leads to the neutronisation of matter through inverse beta decay[11][41]. They are formed at a critical point of core-collapse of a star where the nuclear repulsive force is main support against gravity. Neutron stars have a strong intrinsic magnetic field $\sim 10^{12}\text{G}$ which leads to the formation of a magnetosphere around them[7]. Although the strong magnetic field was measured from the observation of spin down rates of radio pulsars, the origin of the field is an active field of research[9]. These massive neutron stars often form a binary system with other stars and accrete matter from them.

1.2 Accretion in neutron stars

When matter falls onto a compact object, it is acted upon by two major forces - gravitational pull (towards the compact object) and the centrifugal force (away from the compact object). As the matter falls in, gravitational energy is released which in turn is converted into kinetic and thermal energy. If the matter had some angular momentum(J) before getting accreted, it will revolve around the compact object in an orbit where centrifugal force and gravitational force balance each other. On the contrary, if the in-falling matter was at rest initially, there would be a radial inflow of matter. Over time, matter loses angular momentum due to friction and falls closer towards the compact object. This forms an accretion disk around the accreting object. Loss of angular momentum occurs between the differentially rotating layers at different radii. As this proceeds, matter eventually falls onto the compact object.

1.2.1 Effect of the magnetosphere during accretion

A magnetosphere is a space around the Neutron star where the flow of plasma is dominated by the magnetic stress. It extends up to the characteristic Alfvén radius where the magnetic energy density equals the kinetic energy density of the infalling

matter and stops the radial infall of the accreting matter from the companion star. Matter accretes in a thin disk outside the magnetosphere[17]. The outer boundary of the magnetosphere at Alfvén radius which contains ionized gas held by the magnetic field is known as the Alfvén surface. The accreted matter is guided by the magnetic field lines of the neutron star at the Alfvén velocity onto the poles. Due to various plasma instabilities, matter slips into the magnetosphere by diffusion, reconnection of the magnetic field with small-scale fields in the accreting matter or penetration of plasma due to interchange instability[16]. The matter inside the Alfvén radius co-rotates with the star i.e. with angular velocity $\Omega = \Omega_s$, where Ω_s is the angular velocity of the neutron star. Well beyond the Alfvén surface, Ω is Keplerian in the disk and increases inward till a point on the accretion disk where it attains a maximum. Beyond this point, it starts to fall to match Ω_s . This region is known as the transition region where Ω has a maxima and the viscous stress vanishes[17].

The specific angular momentum, l is defined as-

$$l = \frac{J_{in} - J_{out}}{m} = \Omega r^2 - \frac{\eta r^2}{\rho v_r} \frac{d\Omega}{dr} \quad (1.1)$$

where J_{in} is angular momentum imparted by the matter inward, J_{out} is the angular momentum imparted by viscous stress outward, m is the mass of the accreting matter, η is the coefficient of viscosity, ρ is the mass density and v_r is the radial velocity of the accreting matter. l is determined by matching the flow outside the transition region on the disk to the flow in the transition region and then to the flow inside the magnetosphere. Hence, the angular momentum flux is determined, which further determines whether the star spins up or spins down.

Change in the energy of matter passing through the transition zone is equal to the sum of the energy supplied to the exterior flow(due to viscous stress), the energy transmitted into the magnetosphere by magnetic torques and the energy dissipated in the transition layer. More the viscosity more is the dissipation rate and less is the energy supplied to the disk. The rate of change of rotational energy of the star may be written as-

$$\frac{dE_{rot}}{dt} = \dot{M} \left(l\Omega_s - \frac{\Omega_s^2}{2} \frac{M}{I} \frac{dI}{dM} R_g^2 \right) \quad (1.2)$$

From the above equation a parameter ζ is constructed.

$$\zeta = \frac{l}{\Omega_s R_g} \left(\frac{M}{I} \frac{dI}{dM} \right)^{-1} \quad (1.3)$$

Here I is the moment of inertia of the neutron star and R_g is the radius of gyration. Consider $\frac{M}{I} \frac{dI}{dM} > 1$. If $\zeta < 1/2$, $\frac{dE_{rot}}{dt}$ is negative, so the star loses rotational energy and its spin decreases. This is called the spin-down of the neutron star. This is usually satisfied by $l < \Omega_s$ i.e. a fast rotating neutron star. If $\zeta > 1$, star gains rotational energy and starts spinning up. This happens when $l > \Omega_s$ i.e. a slow rotating neutron star. There is one more case, $1/2 < \zeta < 1$ when the star spins down even if rotational energy is increasing. It is a trade-off between the amount of accreted mass and the gain in angular momentum to determine angular velocity.

1.2.2 Accretion torque and pulse period

Let N_{in} be the torque transferred to the star by the magnetic field lines in the inner transition zone of the magnetosphere and N_{out} be the torque transferred by the twisted field lines in the outer transition zone that thread accreting matter and transfer the angular momentum outward. N_{in} and N_{out} spin up and spin down the star respectively. If these two balance on an average, then a more or less constant spin is achieved by the compact star. Accretion torque on such a star then depends on the fluctuations in the accretion rate (\dot{M}) [25]. As \dot{M} increases significantly, Ω_s goes down giving rise to strong spin-up torque to the star. Eventually, when accretion becomes unstable and \dot{M} starts decreasing, Ω_s increases and there is a flip to spin-down torque as spin-up torque falls. Rate of change of sign of angular velocity is an observable phenomenon which gives an idea about mass accretion rate, effective viscosity and angular velocity of the star[14]. Characteristics of mass transfer, the strength of star's dipole field and moment of inertia are predicted from the fluctuation in the pulsation period of the star. Fluctuation in the period can highlight possible reasons such as variation in angular momentum and fluctuations in accretion torque.

In a state where Ω_s reaches an extremely high value, neutron star becomes very unstable (strong spin-up state). It then experiences a braking torque which supports spin down episode without even losing mass from the neutron star[17]. It has been

theorized that during this process gravitational waves are generated[21]. So, to understand this process well, we need to model the accretion process and the structure formed by accretion i.e. accretion mound at the neutron star poles, with a great deal of accuracy.

1.3 Field burial and evolution of neutron stars

The evolution of a neutron star in a binary system has been observed to be different from the solitary pulsars. Pulsars discovered in binary systems were found to have relatively higher spin as compared to the isolated ones[20]. This observation played a significant role in creating an interest in studying the relationship between accretion and the spin of a neutron star. It was proposed by Smarr and Blandford (1976) [42] and Srinivasan and van de Heuvel (1982) [44] that the neutron stars spin up as a result of accretion when they accumulate matter on them and was later confirmed by observation[3]. Another puzzle was introduced when it was discovered that fast-spinning neutron stars have a low magnetic field. Certain theories were proposed to explain this trend. Ideas like spontaneous Ohmic decay was attributed to the field reduction, but later got ruled out due to lack of any clear observational evidence. The theory that was adopted to explain this was the "accretion induced recycling of pulsars"[8]. According to this theory, accretion by a neutron star from its companion in a Roche Lobe overflow spins up the star and diminishes its magnetic field. The term "recycling" highlights the normal pulsars get evolved into fast-spinning millisecond pulsars by accreting matter from their companion [47]. So, it is important to study the accretion process, structures and magnetic field configuration to address the above-mentioned problems.

1.4 Accretion structures on neutron stars

In this thesis, we consider a Neutron star which is the compact object in a high mass X-ray binary (HMXB) system and accretes from the companion star. This matter accretes in a thin disk around the magnetosphere and threads into the magnetosphere by diffusion, recombination or due to Interchange instability.

A strong magnetic field (10^{12}G) constrains the accreted matter(plasma) to move along the field lines to the pole. The size and structure of such a polar cap depend on the size of the magnetosphere and the geometry of mass loading at the accretion disc[2][27]. The infalling matter in the accretion column goes through certain phases: impact, deceleration, accumulation and outflow [40]. It experiences a shock upon entering into the column as it interacts with the pre-existing matter and radiation field. The infalling matter then decelerates due to Coulomb interaction and scattering.

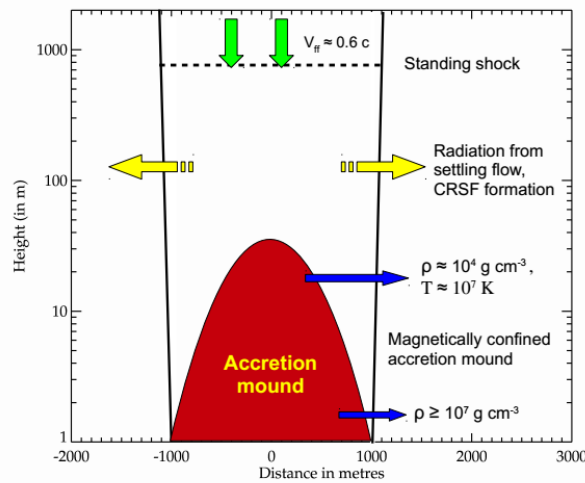


Figure 1.1: Schematic diagram of accretion column and mound at the pole of a neutron star with a radius of 1km and height within 100m. *Source: Dipanjan Mukherjee's PhD thesis, 2014 [31]*

Most of the kinetic energy of infalling matter gets converted into heat and is radiated away. The density of the column increases as the decelerating matter gradually gets accumulated in the region near the bottom of the column. Closer to the stellar surface, very high density makes the gas degenerate. The degeneracy pressure which balances the magnetic pressure at the walls of the column. Matter cools down and gets deposited in the form of a static magnetically confined mountain which is commonly known as accretion mound. Accretion is observed and quantified using X-ray emission from the poles. The bending of field lines can be observed through the cyclotron spectra arising from the resonant scattering of photons by electrons in the strong magnetic field[33].

1.5 Previous work in modelling the mounds

In this section, we discuss and compare the work of Payne et. al, 2004 [38] (PM04, hereafter) and Mukherjee et. al, 2012 [33] (MB12, hereafter) on the modelling of accretion mound. PM04 model the spreading of mound till the equator, having almost 63% of matter restricted to the polar cap at the poles. This happens as a consequence of a distributed mass loading on field lines inside the magnetosphere, resulting in a larger mound as compared to the model proposed by MB12. MB12 consider a more realistic case where the mass loading from the accretion disk is restricted to the edge of the magnetosphere as suggested by theory[17] and simulations(Romanova et. al 2008[39], Kulkarni et. al, 2008[23]). This leads to confinement of the accreted matter to regions around the poles called the polar caps. In case of mounds proposed by PM04, field lines until the equator provide additional lateral pressure to support a larger mass in the elongated polar mound as compared to the mounds proposed by MB12.

Moreover, PM04 consider an isothermal EOS ($p = c_s^2 \rho$) which underestimates the pressure as compared to the degenerate Fermi pressure ($p = k_{ad} \rho^\gamma$) by several orders of magnitude. Higher pressure in degenerate Fermi EOS results in higher plasma beta which makes the system more susceptible to pressure-driven instabilities. Mukherjee et. al, 2013(I)[34] and Mukherjee et. al, 2013(II)[35] argue that the mounds cannot exceed a threshold size as the instabilities in the accreted plasma would lead to mass loss, hence ruling out PM04's proposal of formation of large-scale mound extending up to the equator. Therefore, the model proposed by MB12 is more realistic due to the consideration of non-ideal plasma effects.

In a nutshell, magnetic field lines can drag the matter equatorward as matter keeps accreting. But if matter keeps leaking out simultaneously from the magnetic field confinement near the surface of a neutron star, the formation of a large-scale mound would be hindered.

1.6 Motivation for the thesis

The effect of accretion on the spin and the magnetic field evolution of a neutron star is yet to be understood fully. For a better understanding of the correlation between

accretion and magnetic field evolution, we need to look into what the process of accretion results into and track the evolution of the magnetic field. Moreover, to investigate the hypothesis of field burial i.e reduction of magnetic field line strength induced by accretion, it is necessary to study the effect of accreted matter in the magnetic confinement of the neutron star.

In this thesis, we compare the earlier models and finally follow MB12 to do a detailed analysis of the structure and stability of the magneto-static equations describing the accretion mound. MB12 use a non-relativistic degenerate Fermi equation of state(EOS, hereafter) which describes the mound at the low-density regime of the generalised EOS of Paczyński that captures the behavior of matter in both the relativistic and the non-relativistic regime. Mukherjee (2017) [32] has carried out an analysis showing Paczyński EOS to be more appropriate for the confined matter due to the high densities encountered. We attempt to check the stability of accretion mounds constructed using the Paczyński EOS. We compare the structure and stability of the accretion mounds predicted by both the equations of state. We analyse how the magnetohydrodynamic instabilities develop in response to perturbations and behave as a function of mound height which is directly related to the confined mass.

Chapter 2

Static equilibrium structure of accretion mound

2.1 Introduction

Grad Shafranov (GS, hereafter) equation describes a static, single fluid and ideal magnetohydrodynamic (MHD, hereafter) equilibrium of a magnetically confined axisymmetric plasma obtained by solving the force balance equation,

$$\nabla P = \mathbf{J} \times \mathbf{B} \tag{2.1}$$

where \mathbf{B} is the divergence-free magnetic field and $\mathbf{J} = \frac{1}{\mu_0} \nabla \times \mathbf{B}$ is the plasma current. In this chapter, we discuss the modelling of the structure of an accretion mound and the state of the plasma inside it. We then formulate an equilibrium equation for an accretion mound and highlight the solution and physical inferences.

2.2 Finding equilibrium solution for accretion mound

We consider a mound at equilibrium when there is neither any continued accretion nor non-ideal dissipation effects. It is assumed to contain perfectly conducting fluid with uniform composition. It is bounded at the bottom by a perfectly conducting

rigid crust where magnetic field lines are tied. Single fluid MHD theory applies here. Magneto-static condition is achieved where there exists a hydro-static equilibrium and the field lines are frozen in plasma.

2.2.1 Construction of the Grad Shafranov equation

We consider an axisymmetric cylindrical coordinate system (r, θ, z) to model the accretion mound. As a result of axisymmetry in the system, components of vectors and scalars do not depend on θ . We can decompose the magnetic field of the star into its poloidal and toroidal components. In case of an axisymmetric system, $\mathbf{B}_\theta = 0$. So, $\mathbf{B} = \mathbf{B}_p = \frac{\nabla\Psi \times \hat{\theta}}{r} = \mathbf{B}_z + \mathbf{B}_r$.

$$B_r = -\frac{1}{r} \frac{\partial\Psi}{\partial z} \qquad B_z = \frac{1}{r} \frac{\partial\Psi}{\partial r} \qquad (2.2)$$

where $\Psi = \Psi(r, z)$ is the flux function given by-

$$\Psi(r, z) = \frac{1}{2\pi} \int_{\tilde{r}} \mathbf{B}(\tilde{r}, z) \cdot \mathbf{ds} \qquad (2.3)$$

Ψ is proportional to the total poloidal flux passing through the surface covered by a circle of radius r around the axis of symmetry at a height z . As $\nabla\Psi \cdot \mathbf{B} = 0$, magnetic field can be obtained from the contours of constant Ψ .

The Lorentz force can be written as [24][31],

$$\frac{\mathbf{J} \times \mathbf{B}}{c} = \frac{1}{r^2} \left[\frac{\Delta^2 \Psi}{4\pi} \nabla\Psi + \eta \nabla\eta - ((\nabla\eta \times \nabla\Psi) \cdot \hat{\theta}) \hat{\theta} \right] \qquad (2.4)$$

where $\eta = rB_\theta(r, z)$, $B_\theta(r, z)$ being the toroidal magnetic field component and $\Delta^2 = r \frac{\partial}{\partial r} \left(\frac{1}{r} \frac{\partial}{\partial r} \right) + \frac{\partial^2}{\partial z^2}$ is an Elliptic operator known as the Grad-Shafranov operator..

The Euler equation for a system in static equilibrium is -

$$\nabla p + \rho \nabla\phi = \frac{\mathbf{J} \times \mathbf{B}}{c} = \rho \nabla F \qquad (2.5)$$

where F is a function constant along a flux surface ($\nabla F \times \nabla\Psi = 0$) and ϕ is the gravitational potential. Due to axisymmetry, $\nabla F \cdot \hat{\theta} = 0 \Rightarrow \nabla\eta \times \nabla\Psi = 0$ using equations

2.4. We get the general Grad-Shafranov (GS) equation in cylindrical coordinates as Eq. 2.7 from equations 2.4 and 2.5 -

$$\frac{\Delta^2\Psi}{4\pi}\nabla\Psi + \eta\nabla\eta = -r^2\rho\nabla F \quad (2.6)$$

$$\Delta^2\Psi = -4\pi\eta\frac{d\eta}{d\Psi} - 4\pi r^2\rho\frac{dF}{d\Psi} \quad (2.7)$$

Next we modify Eq. 2.7 to obtain the GS equation for our system of magnetically confined accretion mound on a neutron star. As B_θ and in turn, η are zero in the axisymmetric scenario, using Eq. 2.4 the static Euler equation gets modified into -

$$\nabla p - \rho g + \frac{\Delta^2\Psi}{4\pi r^2}\nabla\Psi = 0 \quad (2.8)$$

We separate the above equation into r and z components which makes it easier for us to solve.

$$\frac{\partial p}{\partial z} - \rho g + \frac{\Delta^2\Psi}{4\pi r^2}\frac{\partial\Psi}{\partial z} = 0 \quad (2.9)$$

$$\frac{\partial p}{\partial r} + \frac{\Delta^2\Psi}{4\pi r^2}\frac{\partial\Psi}{\partial r} = 0 \quad (2.10)$$

Substituting $\frac{\Delta^2\Psi}{4\pi r^2}$ from Eq. 2.10 in Eq. 2.9, we get -

$$\frac{\partial p}{\partial r}\frac{\partial\Psi}{\partial z} = \left(\frac{\partial p}{\partial z} - \rho g\right)\frac{\partial\Psi}{\partial r} \quad (2.11)$$

Eliminating $\frac{\Delta^2\Psi}{4\pi r^2}$ from the above equations, we get,

$$dz\frac{\partial\Psi}{\partial z} = -\frac{\partial\Psi}{\partial r}dr \quad (2.12)$$

Substituting Eq. 2.12 in Eq. 2.11, we get,

$$dz = -\frac{d\rho}{\rho g/c_s^2} \quad (2.13)$$

where $c_s^2 = \gamma p / \rho$. From Eq. 2.12, we get that Ψ is constant. Integrating 2.13, we get

$$gz + \frac{\gamma P}{\rho(\gamma - 1)} = \mathcal{F}(\Psi) \quad (2.14)$$

where $\mathcal{F}(\Psi)$ is the integration constant. Inverting the above equation, density can be obtained as a function of Ψ .

2.2.2 Equation of State of accretion mound plasma

The density profile inside the mound can be determined by solving the Euler equation which depends on the equation of state that relates density and pressure, $p = f(\rho)$.

$$\nabla p + \rho \nabla \Phi = \frac{J \times B}{c} = \rho \nabla F(\Psi) \quad (2.15)$$

where Φ is the gravitational potential and F is a scalar function along a flux surface ($\nabla F \times \nabla \Psi = 0$). Substituting the EOS and re-arranging Eq. 2.15 -

$$\nabla f(\rho) / \rho = \nabla (F(\Psi) - \Phi) \quad (2.16)$$

$$\frac{1}{\rho} \frac{df}{d\rho} \nabla \rho = \nabla (F(\Psi) - \Phi) \quad (2.17)$$

$$\frac{1}{\rho} \frac{df}{d\rho} = g(Z_0(\Psi) - z) + C \quad (2.18)$$

Integrating Eq. 2.17, we get Eq. 2.18 where C is the integration constant and $Z_0(\Psi) = F(\Psi)/g$ is the mound height profile. As the mound height is of the order of few tens of meters and gravitational potential varies by less than 1% in this region[33], $\nabla \Phi = gz$ is a good approximation where $g = 1.86 \times 10^{14} \text{ g/cm}^2$ is the gravity at the crust of the neutron star. We evaluate the density profile for different EOS using Eq. 2.18.

2.2.3 Isothermal EOS

For an isothermal EOS, $p = c_s^2 \rho$, where $c_s^2 = k_B T / (\mu_e m_p)$, $\mu_e = 2$ is the mean atomic weight per electron, m_p is the mass of a proton and $T \simeq 10^7 K$ is the temperature

inside the mound[38]. The density profile is given as

$$\rho = \rho_0 \exp[(Z_0(\Psi) - z)/h_{iso}] \quad (2.19)$$

where $h_{iso} = c_s^2/g$ is the isothermal scale height and $C = h_{iso} \ln \rho_0$. While this EOS has been employed in PM04, we do not use it in our work as it causes an under-estimation of pressure and hence over-estimation of confined mass in the mound.

2.2.4 Non-relativistic Degenerate Fermi EOS

For a polytropic EOS, $p = k\rho^\gamma$ where γ is the adiabatic index. After integrating, the density profile turns out to be

$$\rho = \left(\frac{g(\gamma - 1)}{\gamma k} \right)^{1/(\gamma-1)} (Z_0(\Psi) - z)^{1/(\gamma-1)} \quad (2.20)$$

where $C = 0$.

The choice of EOS is crucial for determining the mound structure and is determined by the maximum density inside the mound and the properties of the accreted plasma. The state of matter is characterised by the electrostatic coupling parameter Γ [15] [26]-

$$\Gamma = \frac{Z^2 e^2}{k_B T} \left(\frac{4\pi n}{3} \right)^{1/3} \quad (2.21)$$

The plasma becomes liquid for density $\sim 10^8 \text{ g/cm}^3$ near the base of the mound where $\Gamma \simeq 1$ and solidifies when density increases further making $\Gamma \geq 173$. The degenerate matter must have a maximum density less than 10^8 g/cm^3 inside the mound above the base for it to be in a gaseous form. This kind of matter would contribute to the plasma pressure, majorly due to the degenerate electrons if $T_F > T$, T_F being the Fermi temperature i.e. degeneracy pressure will be dominant at depths where the plasma is cooler than T_F ,

$$T_F = \frac{m_e c^2}{k_b} (\sqrt{x_F^2 + 1} - 1) \quad (2.22)$$

where $x_F = p_F/(m_e c)$ and $p_F = (\frac{3h^3}{8\pi\mu_e m_p})^{1/3} \rho^{1/3}$ is the Fermi momentum.

From X-ray observations [12][6] of strongly magnetised pulsars, it is found that $T \sim 5 - 10$ keV in the hotspot. We need to find the density at which $T_F > 10$ keV to map the region where degeneracy pressure dominates. As per the calculations carried out by MB12 by inverting Eq. 2.22, for $T_F = 10$ keV $\rho = 1.54 \times 10^4$ g/cm³ which occurs at a depth of $0.01Z_0(\Psi)$ from the top. Density increases up to the order of 10^6 g/cm³ as we go further into the mound and T_F , in turn, will exceed 10 keV. Hence, in the majority of the mound $T \ll T_F$ making the mound being constituted of degenerate plasma. As degeneracy pressure is dominant over the thermal pressure, for the modelling of the equation of state of the mound, we apply the pressure for degenerate Fermi gas at $T = 0$ as

$$p = \frac{\pi m_e^4 c^5}{3 h^3} \left(x_F(x_F + 1)^{1/2}(2x_F^2 - 3) + 3 \ln(x_F + \sqrt{1 + x_F^2}) \right) \quad (2.23)$$

This pressure can be represented in the form of $p = k\rho^\gamma$ for both relativistic($x_F \ll 1$) and non-relativistic($x_F \gg 1$) plasma. γ is evaluated as $\frac{d \ln p}{d \ln \rho}$.

$$\gamma = \frac{8}{5} \left(x_F(x_F^2 + 1)(2x_F^2 - 3) + 3(1 + x_F^2)^{1/2} \ln(x_F + \sqrt{1 + x_F^2}) \right)^{-1} \quad (2.24)$$

For $\rho < 10^7$ g/cm³, γ asymptotically tends to 5/3. If we consider the matter inside the mound to be in the gaseous phase, then the maximum densities are $< 10^7$ g/cm³. Hence, in that limit the EOS becomes

$$p = 3.122 \times 10^{12} \rho^{5/3} \text{ dynes/cm}^2 \quad (2.25)$$

2.2.5 Paczyński EOS

The description of the EOS through a single polytrope as in Eq. 2.25 does not cater to the matter with a density greater than 10^7 g/cm³ near the crust of the neutron star, hence it cannot be used as a generalised EOS to model the whole mound. A

better approximate description of Fermi pressure was proposed by Paczyński [37] as

$$p = \frac{\pi m_e^4 c^5}{3 h^3} \frac{8/5 x_F^5}{(1 + 16/25 x_F^2)^{1/2}} \quad (2.26)$$

In this EOS, γ asymptotes to $4/3$ for $\rho < 10^7$ i.e. $x_F \ll 1$ and $5/3$ for $\rho > 10^7$ i.e. $x_F \gg 1$. Besides, it matches the Fermi pressure to within $\leq 1.8\%$ [32]. Now using Eq. 2.18, density profile is calculated for this EOS.

$$x_F = \frac{5}{4} \left(\frac{\xi^2 - 8/3 + \xi \sqrt{16/9 + \xi^2}}{32/9} \right) \quad (2.27)$$

where $\xi = \frac{16}{15} \frac{\mu_e m_p}{m_e c^2} (Z_0(\Psi) - z) + 1$

2.3 Solving GS equation

Different parameters in quantifying this physical phenomena are as follows-

- A neutron star of mass $1.44 M_\odot$ and radius 10km
- Axisymmetric cylindrical coordinate system (r, θ, z) with the origin at the base of a polar cap of radius 1km (adapting the model proposed by [33])
- The initial magnetic field when accretion has not happened is a uniform dipolar field along z given as $\mathbf{B}_d = B_0 \hat{z}$ where $B_0 = 10^{12} \text{G}$. As the mound heights are within 100m the local unloaded dipolar magnetic field can be approximated to a uniform field.
- Newtonian gravitational field is considered. Acceleration due to gravity g is given by -

$$\begin{aligned} \mathbf{g} &= \frac{GM}{R^2} \\ &= -1.86 \times 10^{14} \left(\frac{M_*}{1.4M_\odot} \right) \left(\frac{R_*}{10} \right)^{-2} \text{cm s}^{-2} \hat{z} \end{aligned} \quad (2.28)$$

- Accreted plasma is assumed to be in a polytropic state, $p = k_{ad} \rho^\gamma$.

- Using Eq. 2.20 we get the density profile for the accreted gas in the polytropic EOS

$$\rho = A[Z_0(\Psi) - z]^{\frac{1}{\gamma-1}} \quad (2.29)$$

where $A = [g(\gamma - 1)/(\gamma k_{ad})]^{\frac{1}{\gamma-1}}$ and $Z_0(\Psi)$ is the mound height profile as a function of the flux coordinate Ψ .

- The values of P , ρ and their derivatives are set to vanish at the maximum height of the mound i.e. matter density above the mound falls with height z and becomes almost negligible in comparison to the mound.

Substituting Eq. 2.29 in Eq. 2.8, we get the **Grad-Shafranov** equation for a magnetically confined accretion mound with non-relativistic degenerate Fermi gas as-

$$\frac{\Delta^2 \Psi}{4\pi r^2} = -\rho(\Psi)g \frac{dZ_0(\Psi)}{d\Psi} \quad (2.30)$$

The mound height profile is chosen as -

$$Z_0 = Z_c \left(1 - \left(\frac{\Psi}{\Psi_p} \right)^2 \right) \quad (2.31)$$

where Z_c is the maximum central height of the mound and Ψ_p is the maximum value Ψ can take inside the mound. $Z_0(\Psi)$ is an analytic differentiable function of Ψ [19]. Here we have considered a parabolic profile of the mound in Ψ . Although a hollow mound profile, e.g.

$$Z_0(\Psi) = \frac{Z_c}{0.25} \left(0.25 - \left(\frac{\Psi}{\Psi_p} - 0.25 \right)^2 \right) \quad (2.32)$$

may be more realistic [33], a filled mound is also shown to represent the system quite reasonably for the purpose of investigating instabilities [35].

We solve the GS equation numerically and report our results for different equations of state in this section. Numerical methodology used for solving the second-order elliptic GS equation is described in Appendix A.

2.3.1 GS solutions for degenerate non-relativistic plasma

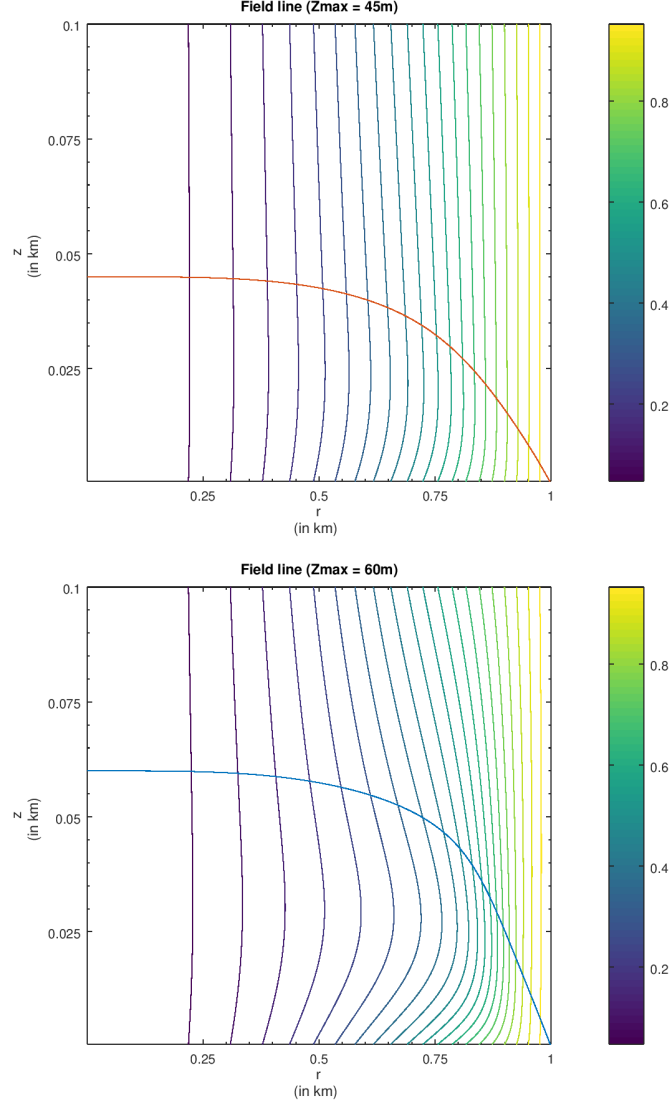


Figure 2.1: Ψ -profile for $Z_c = 45\text{m}$ (top) and $Z_c = 60\text{m}$ (bottom) in units of 0.5×10^{12} . The colorbar shows values of magnetic field flux. The solid lines over-plotted in red and blue across the contour show the top boundary of the mound.

We have used the framework of MB12 to formulate and solve the GS equation for the accretion mound of a neutron star. This problem has been approached by Hameury et. al 1983 [19] where they had considered ultra-relativistic EOS with $\Gamma = 4/3$ which models the high-density matter ($\rho \geq 10^7 \text{g/cm}^3$) present near the base of the mound.

They also used $\mu_e = 1$ plasma which corresponds to pure hydrogen composition. But in case of a neutron star with a strong magnetic field, stable thermonuclear burning will produce mixed ash for which $\mu_e = 2$ is more accurate [10]. These shortcomings are addressed by MB12 by considering a degenerate non-relativistic EOS for a $\mu_e = 2$ plasma as mound densities in the polar caps are mostly less than 10^6g/cm^3 .

Z_c (in meters)	Mass (in M_\odot)	Max density (in g/cm^3)
45	0.52×10^{-12}	3.5×10^7
60	1.23×10^{-12}	5.4×10^7
70	2.17×10^{-12}	6.8×10^7

Table 2.1: The maximum mass and density obtained from GS solution for different mound heights. For a magnetic field of $\sim 10^{12}G$, a degenerate non-relativistic Fermi mound can confine matter upto a threshold height of $\sim 72\text{m}$.

In [Figure 2.1](#), we have plotted the field line profile of mounds of height 45m and 60m. The contours of constant flux represent the magnetic field lines. The magnetic field lines, tied to the crust, move outwards from their initial configuration to support the lateral movement of matter in the mound. Tension develops in the field lines which supports the gas pressure gradient in the horizontal direction ($\nabla p = \mathbf{B} \cdot \nabla \mathbf{B}$). The distortion of field lines increases with a larger base density as it gives rise to larger pressure which in turn requires more curvature in field lines to balance the pressure gradient. This leads to bunching of field lines and increased field strength. This can be observed in [Figure 2.1](#) where the field line curvature is more for the $Z_c = 60\text{m}$ mound as compared to the $Z_c = 45\text{m}$ mound. But, for a given field strength a mound can confine matter up to a maximum height. Beyond that threshold, the GS solution does not converge and there is a loss of equilibrium. A field strength of $B_0 = 10^{12}G$ can confine mounds up to a height of around 72m.

2.3.2 GS solution with Paczyński EOS

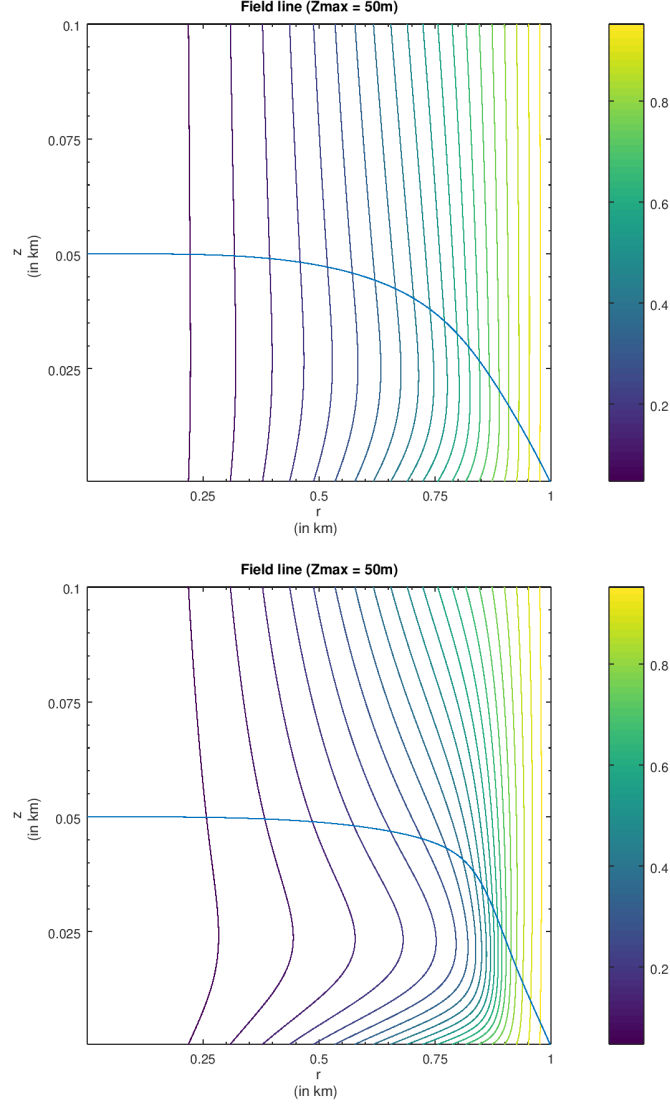


Figure 2.2: Ψ -profile for $Z_c = 50\text{m}$ in degenerate non-relativistic EOS (top) and $Z_c = 50\text{m}$ in Paczyński EOS (bottom) in units of 0.5×10^{12} . The colorbar shows values of magnetic field flux. The solid lines over-plotted in blue across the contour show the top boundary of the mound.

At the base of the mound, the density increases up to the order of magnitude of 10^7g/cm^3 . So, the Paczyński EOS can describe the Fermionic pressure in this domain of density with better accuracy. We keep the same initial dipolar field configuration

tied to the crust and the other peripheral boundaries as in the mound with non-relativistic EOS. We just change the expression for pressure to the general degenerate Fermi pressure at $T = 0$. [Figure 2.2](#) shows the comparison between field line profile of mounds of height 50m for a degenerate non-relativistic EOS and Paczyński EOS. The base densities and confined mass are higher for a Paczyński solution than the non-relativistic EOS. As a smaller mound for Paczyński EOS can hold more mass, the threshold height for stability for the same magnetic field strength is as low as ~ 50 m as compared to ~ 70 m in degenerate non-relativistic EOS. Mass of a 40m high mound with Paczyński EOS is $2.993 \times 10^{-12} M_{\odot}$ and with non-relativistic degenerate Fermi EOS is $0.384 \times 10^{-12} M_{\odot}$. This topic is taken up further in [chapter 4](#).

2.4 Discussion

In this chapter, we have modelled the density and magnetic field profile of an accretion mound by solving the GS equation. The accretion profile at the edge of the magnetosphere determines the mass-loading of the field lines threaded to the accretion disk, which in turn determines the shape of the mound. The magnetic field configuration is determined by the mound morphology. We have assumed a parabolic profile which has a maximum mass at the central part and the mass falls towards the edge. Starting with this initial guess for the mound shape, we computed the equilibrium mound structure for different equations of state: a non-relativistic degenerate Fermi EOS and Paczyński EOS. The magnetic field lines distort from the initial dipolar structure to confine the accreting matter and prevent its spreading towards the equator. This restricts the growth of the mound up to a threshold height for a given magnetic field strength. We also observed that the Paczyński mounds which involve relativistic characteristics for degenerate plasma, confine more matter and hence reach a lower threshold height as compared to the non-relativistic degenerate Fermi mounds.

Chapter 3

Stability analysis of accretion mounds in 2D

3.1 Introduction

Having obtained a numerical solution of the GS equation for an accretion mound as explained in [chapter 2](#), we analyse the stability of the equilibrium in this chapter. We import the GS solution into the PLUTO MHD code (Mignone et. al, 2007 [[30](#)]) and evolve it as per the magnetohydrodynamics equations in time. We discuss the problem setup in PLUTO, the initial conditions, boundary conditions and the choice of the equation of state for the simulations.

Once we establish the stability of the solution, we perturb the solution to investigate the local dynamics and to look for instabilities in the mound. We devise different ways of adding perturbation to excite physical effects at various length and time scales. We add zero-mean density perturbations (no extra mass added) i.e. re-arrange the matter in the mound to study the pressure-driven instabilities. We also add non-zero mean density perturbation (extra mass) to the mound to analyse the gravity-driven modes. In this chapter, we perform the analysis on a mound with non-relativistic degenerate Fermi plasma and discuss the stability analysis with the generalised EOS of Paczynski in [chapter 4](#).

3.2 Numerical setup using PLUTO

PLUTO is a Godunov scheme [45] based tool to solve conservation equations of gas dynamics (coupled hyperbolic and parabolic PDEs) numerically. The code supports varieties of Riemann solvers, time-stepping and reconstruction algorithms that are compatible with different physics modules (HD, MHD, RHD, RMHD) aiming to solve a plethora of astrophysical problems. It integrates the coupled conservation equations numerically and evolves the physical quantities in time, using the initial and boundary conditions provided in terms of the primitive variables $\{\rho, \mathbf{v}, p, \mathbf{B}\}$. A conservation equation is of the form -

$$\frac{\partial U}{\partial t} + \nabla \cdot \mathbf{T}(U) = S(U) \quad (3.1)$$

where U is any conservative variable, $\vec{T}(U)$ is the flux tensor of the corresponding variable and $S(U)$ is the source term. Using the solutions for primitive variables, conservative variables $\{\rho, \rho\mathbf{v}, E, \mathbf{B}\}$ can be defined, for example, total energy $E = \rho\epsilon + \rho\mathbf{v}^2 + \mathbf{B}^2/2$. Shocks and rarefactions are expressed in terms of primitive variables. Moreover, it is better to implement the limiters on primitive rather than the conservative variables as positivity of density and pressure can be directly checked in each zone of the computational domain while integrating. By using the approach of solving Riemann problem by finite volume method, PLUTO can handle discontinuities and shock waves in fluid flows[5]. A Riemann problem is an initial value problem composed of conservation equations with discontinuity. It is used as a sample problem to build numerical schemes.

3.2.1 MHD Equations and numerical schemes in PLUTO

In this work, we use PLUTO's MHD module which solves the Equations 3.2 - 3.5. These equations are a combination of Navier-Stokes equations of fluid dynamics and Maxwell's equations of electrodynamics.

$$\frac{\partial \rho}{\partial t} + \mathbf{v} \cdot \nabla \rho + \rho \nabla \cdot \mathbf{v} = 0 \quad (3.2)$$

$$\frac{\partial \mathbf{v}}{\partial t} + \mathbf{v} \cdot \nabla \mathbf{v} + \frac{1}{\rho} \mathbf{B} \times (\nabla \times \mathbf{B}) + \frac{1}{\rho} \nabla p = \mathbf{g} \quad (3.3)$$

$$\frac{\partial \mathbf{B}}{\partial t} + \nabla \times (\mathbf{v} \times \mathbf{B}) = 0 \quad (3.4)$$

$$\frac{\partial p}{\partial t} + \mathbf{v} \cdot \nabla p + \rho c_s^2 \nabla \cdot \mathbf{v} = 0 \quad (3.5)$$

where $\mathbf{g} = g \hat{\mathbf{z}}$ is the constant acceleration due to gravity and c_s^2 is the square of sound speed. \mathbf{B} has been normalised by a factor of $1/\sqrt{4\pi}$. Eq. 3.2 is the continuity equation which comes from mass conservation. Eq. 3.3 is the Euler equation (momentum conservation) which is derived using force balance condition. Eq. 3.4 shows the induction equation which is derived from Faraday's law. Eq. 3.5 uses the energy conservation principle where p is related to energy as $E = p/(\gamma - 1) + \rho \mathbf{v}^2/2 + \mathbf{B}^2/2$. PLUTO (v.4.3 June 2018, used in the thesis) incorporates modules to add dissipative factors like viscosity, resistivity, thermal cooling, forced turbulence and magnetic diffusivity to the ideal MHD setup.

Spatial reconstruction is carried out in primitive or characteristic variables using high order interpolation methods like Piece-wise Parabolic Method (PPM), linear Total Variation Diminishing (TVD) limiting or Weighted Essentially Non-Oscillatory (WENO) [30]. PLUTO provides a block-structured adaptively refined grid (Adaptive Mesh refinement). This modular structure helps in the implementation of a conservative finite volume discretization which evolves zone averages in time using Corner-Transport-Upwind method (CTU). PLUTO carries out numerical integration of conservation laws through shock capturing-schemes using this finite volume method. This scheme is second-order accurate in space and time and reduces the numerical error arising from a sharp gradient in physical quantities.

Numerical errors can inevitably lead to unphysical features like monopoles ($\nabla \cdot \vec{B} \neq 0$) in the simulation. Hence, divergence cleaning is implemented using Extended Generalised Lagrange Multiplier (EGLM) to make the divergence zero explicitly. This technique adds the divergence equation ($\nabla \cdot \vec{B} = 0$) as a constraint to the MHD equations while solving them. This preserves the constraint condition up to high accuracy [4].

$$\frac{\partial(\rho\vec{v})}{\partial t} + \nabla \cdot \left[\rho\vec{v}\vec{v} - \vec{B}\vec{B} + \vec{I}\left(p + \frac{B^2}{2}\right) \right] = -(\nabla \cdot \vec{B})\vec{B} + \rho\vec{g} \quad (3.6)$$

$$\frac{\partial E}{\partial t} + \nabla \cdot \left[\left(E + p + \frac{B^2}{2} \right) \vec{v} - (\vec{v} \cdot \vec{B}) \vec{B} \right] = -\vec{B} \cdot \nabla \Psi \quad (3.7)$$

$$\frac{\partial \vec{B}}{\partial t} + \nabla \cdot (\vec{v} \times \vec{B}) = -\nabla \Psi \quad (3.8)$$

$$\frac{\partial \Psi}{\partial t} + c_h^2 \nabla \cdot \vec{B} = \frac{-c_h^2}{c_p^2} \Psi \quad (3.9)$$

where c_h is the maximum allowed speed of the local characteristics, $c_p = \sqrt{\Delta l_{min} c_h / \alpha}$ is the diffusion coefficient and Ψ is the generalised Lagrange multiplier. This leads to the natural evolution of the system towards a divergence-less state.

3.2.2 Choice of equation of state

PLUTO provides a pool of equations of state including IDEAL (pressure as a function of density and temperature), ISOTHERMAL (pressure as a function of density only), PVTE law (internal energy as a function of temperature and chemical potential, used to study a partially ionized hydrogen gas in local thermodynamic limit), TAUB EOS (adiabatic index is a function of temperature, $\gamma \rightarrow 5/3$ at low temperature and $\gamma \rightarrow 4/3$ at high temperature, describes relativistic perfect gas). We modify the ISOTHERMAL EOS into another form of BAROTROPIC EOS (degenerate non-relativistic Fermi plasma) to model the matter inside the accretion mound in neutron stars in the MHD regime. An EOS of a degenerate non-relativistic Fermi plasma is used.

$$P = k_{ad} \rho^{5/3} \quad k_{ad} = \left(\frac{(3\pi^2)^{2/3}}{5} \right) \left(\frac{\hbar^2}{m_e (\mu_e m_p)^{5/3}} \right) \quad (3.10)$$

This above equation suggests

$$\frac{\partial}{\partial t} \left(\frac{P}{\rho^\gamma} \right) = 0 \quad (3.11)$$

where $\gamma = 5/3$ is the ratio of specific heats in the non-relativistic limit. Addition of thermal or kinetic energy does not alter the pressure. With a time independent pressure, the energy equation and is not required to be solved for this EOS.

3.3 Problem set up in PLUTO

Without perturbations, the equilibrium solution derived from the GS solution should remain immutable over time. Numerical errors, may, however, cause the solution to evolve. To estimate this, we check the stability of the GS solution by evolving it in time. Stability will be established if the solution remains static over a significant timescale. We shall carry out the perturbation analysis only after confirming equilibrium. We set up an environment in PLUTO according to the conditions in which the GS equation was solved.

Integration scheme	RK3
Spatial interpolation	PPM
Riemann solver	HLL, TVDLF

Table 3.1: List of numerical schemes chosen in PLUTO best suited for the problem in this thesis

Given a set of initial system conditions and boundary specifications, PLUTO can evolve the system in time based on the underlying magneto-hydrodynamic conservation equations. We use the following computational framework and square cells ($\Delta r \simeq \Delta z$) to reduce numerical error. High (third) order integration (Runge Kutta-RK3) and interpolation (Piecewise Parabolic Method-PPM) schemes are used to enhance accuracy. TVDLF and HLL are chosen as they are less diffusive Riemann solvers.

3.3.1 Initial condition

We choose a small patch inside the mound as our computational domain as shown in [Figure 3.1](#) where we seek to establish the stability of equilibrium. The region is cho-

Physical parameters	Normalization constants
Density (ρ_0)	10^6 g/cm^3
Length (L_0)	10^5 cm
Magnetic field (B_p)	10^{12} G
Velocity (v_0)	$2.82 \times 10^8 \text{ cm/s}$
Time (t_0)	$3.55 \times 10^{-4} \text{ s}$

Table 3.2: The normalization factors for density, length and magnetic field are fed into PLUTO maintaining consistency with the GS solution

sen such that the local Alfvén speeds are non-relativistic. We feed in the equilibrium solution obtained from the GS equation as an initial condition to PLUTO. The physical variables $\{\rho, \vec{v}, p, \vec{B}\}$ are normalized in PLUTO and interpolated on the chosen grid. These physical quantities are non-dimensionalized by introducing dimensioned normalization factors. The normalization for density(ρ_0), length(L_0) and magnetic field(B_0) used while solving GS equation are supplied to PLUTO.

Dynamics in strongly magnetised plasma is characterised by the Alfvén waves (low-frequency oscillations propagating in the system). Hence, velocity and time are normalized with the Alfvén velocity ($v_A = B_p/\sqrt{4\pi\rho_0}$) and Alfvén time ($t_A = L_0/v_A$) of the system. For the stability checking, we import the GS solution for the degenerate non-relativistic mound, discussed in [chapter 2](#). Normalised density and magnetic field are imported into PLUTO. Initial pressure is computed from imported density as $p = k_{ad} \rho^\gamma$. Initial velocities are set to zero.

3.3.2 Boundary condition

We have set the boundary of the computational domain to be fixed to its initial values. We claim that if the solution is static i.e. there is no inflow or outflow within the chosen box, then it doesn't affect the dynamics of its neighbouring region and hence equilibria must hold throughout the mound. For the implementation of a fixed boundary, $Q = Q_0$ and $\nabla Q = \nabla Q_0$.

3.3.3 Equation of state

We choose to use a barotropic EOS as pressure and density are uniquely related ($p = k_{ad} \rho^{5/3}$) in non-relativistic degenerate Fermi EOS. This is set up by modifying

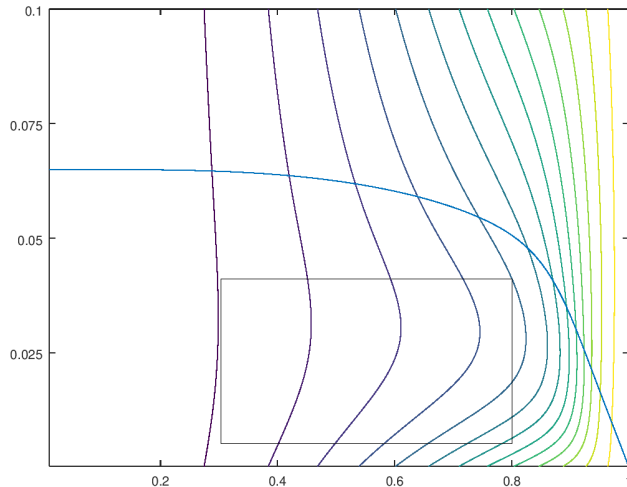


Figure 3.1: A Computational domain in PLUTO. A region is chosen well inside the mound to obtain the numerical error in the equilibrium solution devoid the the numerical artefacts due to boundary effects. Similar domains as mentioned in [Table 3.3](#) are chosen for getting a better error limit.

PLUTO's isothermal EOS module which is also of the barotropic form ($p = c_s^2 \rho$). As pressure is not an independent variable anymore ($p = p(\rho)$), the energy equation becomes redundant [29].

With the setup described above, we check for stability by considering different computational domains throughout the mound. We budget for the maximum error that we encounter closer the boundary. This is necessary to decide the order of magnitude of perturbations (which should be higher than the numerical error at machine precision) in later work to study instabilities.

3.4 Checking the stability of equilibrium solution using PLUTO

While dynamically evolving the equilibrium solution obtained by solving GS equation using PLUTO, we check the amount of change in the mound density profile from the equilibrium with time. We want to quantify these numerical inaccuracies and claim

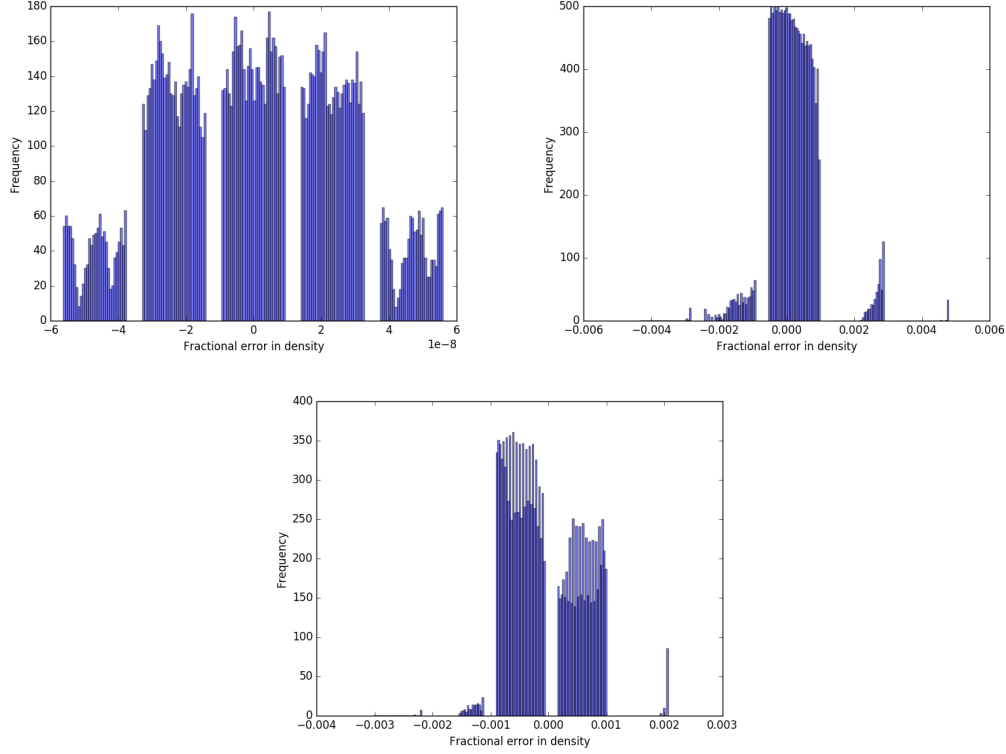


Figure 3.2: Histograms show the error distribution in density of a $Z_c = 60m$ mound at $t = 0$ (top left) showing error close to zero at $t = 50t_A$ (top right) showing maximum error within 0.4% and at $t = 100t_A$ (bottom) showing maximum error within 0.2% in region 6 as per [Table 3.3](#)

that the equilibrium can be considered stable only up to a certain error limit. An additional check on the stability of equilibrium can be done, if upon introducing small random perturbations ξ in velocity or density field such that $\langle \xi \rangle = 0$ and evolving, the initial solution doesn't change.

We consider an accretion mound of $Z_c = 60m$. First, we calculate the over-density, $(\rho[t] - \rho[t = 0])/\rho[t = 0]$ at each grid point to study the evolution of deviation of density from equilibrium with time. We evolve it until $100 t_A$. We analyze the areas near the boundaries of the mound.

The error mostly lies in a range of up to 1% around zero. But at the top-right edge, numerical artefacts are more prominent as the value of the physical quantities is smallest in the computational domain. Hence, the histograms show a comprehensive

picture of the error distribution with the majority of the peaks around zero and a very few peaks at maximum percentage errors (about one order of magnitude higher). Table 3.3 presents the maximum error in overdensity closer to the boundary regions of the mound.

Error at $100t_A$ is higher than the error at $5t_A$ due to building up of numerical error through the computation time. In addition, the maximum internal flow velocity ($v_{max} \sim 10^4\text{m/s}$) is less than 1% of the local Alfvén velocities ($\sim 10^8\text{m/s}$). If we extend the computational domain beyond these regions, we move closer to the boundary, hence we get an error higher than other regions by at least an order of magnitude. Maximum fluctuation in over-density after $100 t_A$ approaches 0.3% when chosen away from the boundaries. We choose the region (6) for perturbation analysis as it is the region with less error and covers the region where magnetic field lines are bent the most. Higher curvature of the field lines makes the system more prone to instabilities like kink, interchange etc. Hence, we choose this region for further analysis.

Region	r-range (in km)	z-range (in km)	% error _{max} $t = 5t_A$	% error _{max} $t = 100t_A$	v_{max} at $t = 100t_A$ (in $2.82 \times 10^4\text{cm/s}$)
1	0.008 – 0.50	0.001 – 0.05	0.0075	0.042	0.56
2	0.25 – 0.65	0.03 – 0.05	0.018	0.28	3.2
3	0.3 – 0.7	0.02 – 0.04	0.16	0.35	1.0
4	0.5 – 0.95	0.001 – 0.008	0.24	0.15	7.2
5	0.007 – 0.3	0.042 – 0.0588	0.048	0.9	2.7
6	0.3 – 0.8	0.01 – 0.04	0.01	0.28	4.3

Table 3.3: Error in density over evolution through $t = 0.0$ to $t = 100t_A$ in different regions as close to the boundary as possible on all sides of a mound with $Z_c = 60\text{m}$

With error less than 1% in all the chosen regions, we have a preliminary conclusion that the equilibrium solution obtained is stable and it can be used for further perturbation analysis studies. In the next section, we report the results from adding zero mean velocity perturbations ξ i.e. $\langle \xi \rangle = 0$. This ensures that no centre of mass velocity and no excess mass has been added to the mound matter. As no additional mass is added to the computational region at equilibrium, there is no change in the

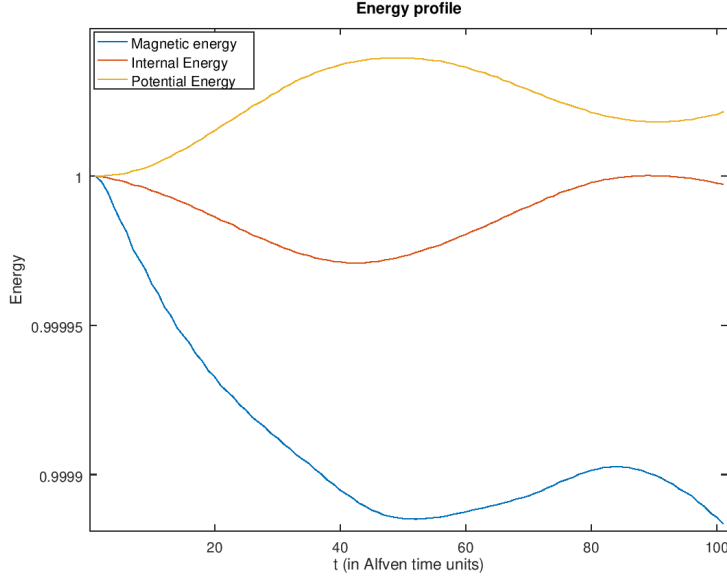


Figure 3.3: Normalised magnetic, internal and potential energy for the equilibrium solution of $Z_c = 60m$. The values of the energy are normalized to their initial values *i.e.* $E_{mag}(t) \rightarrow E_{mag}(t)/E_{mag}(0)$, $E_{int}(t) \rightarrow E_{int}(t)/E_{int}(0)$ and $E_{pot}(t) \rightarrow E_{pot}(t)/E_{pot}(0)$

internal energy and pressure becomes a function of density only. So, we use the non-relativistic degenerate Fermi (a barotropic form) equation of state.

The evolution of magnetic energy (E_{mag}), internal energy (E_{int}) and potential energy (E_{pot}) of the section of the mound through $100t_A$ has been plotted in [Figure 3.3](#). The energies fluctuate during the evolution and end up within 0.1% error at $100t_A$ which can be attributed to the built up numerical artefacts. This constancy in energy also hints at the stability of the GS solution.

3.4.1 Adding velocity perturbations

Being aware of the error values near boundaries of the mound, we first choose a computational region away from the boundary to avoid related numerical artefacts. We carefully choose a region capturing the curved field lines, to carry out the perturbation analysis. Keeping in mind the error threshold for an equilibrium solution in the chosen computational domain, next, we perturb the velocity field in a central region kept away the boundary to study their evolution in the spatial domain.

3.4. Checking the stability of equilibrium solution using PLUTO

Z_c (in meters)	Perturbation Strength	Max % error $t = 5t_A$	Max % error $t = 100t_A$
45	5	1.0	0.5
	10	2.0	1.2
	15	2.8	2.0
	20	4.0	3.2
60	5	1.2	0.24
	10	1.5	0.5
	15	3.2	0.8
	20	4.0	1.0
70	5	0.6	0.2
	10	1.2	0.4
	15	1.8	0.42
	20	2.5	0.55

Table 3.4: Error in density due to zero mean velocity perturbation is shown at $t = 5t_A$ and $t = 100t_A$ in mounds of different heights while evolving the system through $100t_A$

To perturb any physical quantity at equilibrium, we add a normalized perturbation field $\xi(r, z)$ as follows -

$$Q = Q_0(1 + \eta\xi(r, z)) \quad (3.12)$$

where η is the perturbation strength and $\xi(r, z)$ is a random value assigned at each grid point in the perturbation zone such that $\langle \xi \rangle = 0$ such that the centre of mass remains stationary. Serious numerical artefacts can arise due to sharp gradients in the edges of the perturbed region. So, we smoothen the cells in the perturbed region using some exponential functions. The following expression depicts the smoothing-

$$Q_{ptb} \rightarrow Q_{ptb}(1 - \exp(-z/z_{norm}))(1 - \exp(-r/r_{norm})) \quad (3.13)$$

where Q_{ptb} is the perturbation introduced to physical quantity Q , (r, z) are the cylindrical coordinates and (r_{norm}, z_{norm}) are the normalization constants on respective coordinates.

We want to understand the dynamics of the instabilities as we transition from mounds of lower height and mass ($Z_c < 60m$) to higher ones ($Z_c \sim 72m$) beyond which the GS solution does not converge. For mounds of height 45m, 60m and 70m, we track the evolution of the perturbation till $100t_A$ and report the maximum overdensity values for different perturbation strength (η) such as 5%, 10%, 15% and 20% in [Table 3.4](#). As

mentioned in the previous section, the distribution of error lies close to zero within 1% – 2% although a few grid points might have larger error values which do not significantly affect the stability in the region. It is observed that there is a motion of the plasma in the perturbed region due to the introduced non-zero velocity. This leads to the formation of pockets of excess matter at some grid points and less dense voids at others as shown in the middle panel of Figure 3.4. Eventually, the over-dense packets spread out as shown in the bottom-most panel of Figure 3.4.

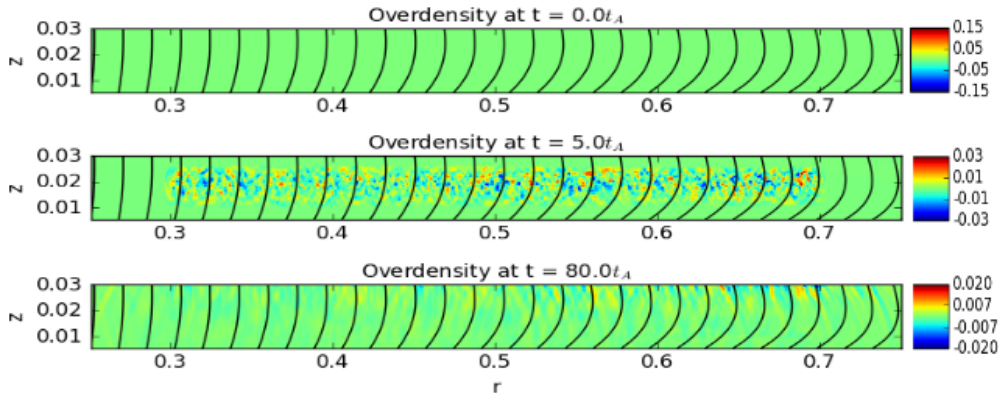


Figure 3.4: Over-density profiles of a mound with $Z_c = 45m$ and velocity perturbation strength of 15% at different time steps

This makes the system return to an energy state close to equilibrium as shown in Figure 3.5(top) where flow velocities are reduced by more than three orders of magnitude at $t = 100t_A$. But such perturbations do add non-zero kinetic energy to the system. Introducing perturbation of strength more than 20% makes the system depart from equilibrium and creates a pressure imbalance which manifests in magnetic field line distortion. This is shown in Figure 3.5(bottom) as the normalised magnetic energy increases by more than an order of magnitude in comparison to the scenario in Figure 3.5(top) where perturbation strength is 5%. So, velocity perturbation is a good parameter to check the stability of the equilibrium for a small η (up to 20%). It helps to probe the pressure-driven instabilities in toroidal modes as performed in Mukherjee et. al (2013)[34][35]. In 3D, they can excite linear modes with even a small $\eta \sim 2\%$.

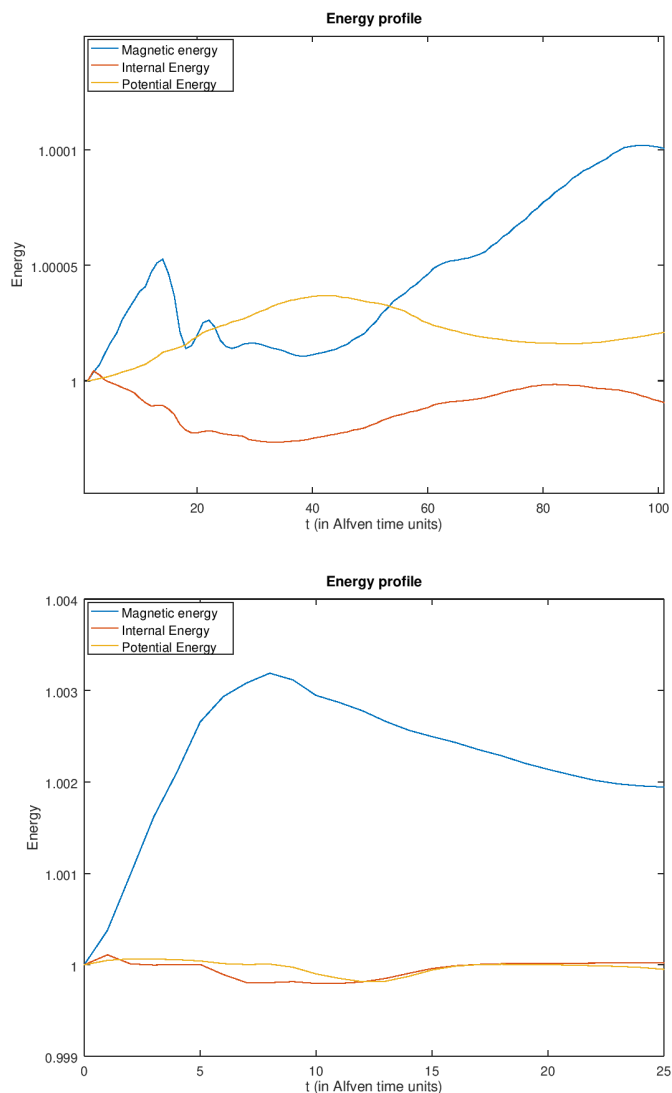


Figure 3.5: Normalised magnetic, internal and potential energy for the equilibrium solution of a $Z_c = 60\text{m}$ mound with 5% (top) and 50% (bottom) velocity perturbation

3.4.2 Adding density perturbation

With the analysis of velocity perturbation, we realise that beyond a threshold, the excessive kinetic energy disturbs the equilibrium by distorting magnetic field lines. Another method of verifying stability is by adding zero-mean $\langle \xi \rangle = 0$ density perturbations. It physically represents local re-arrangement of matter inside the perturbed

zone and does not enhance the energy of the mound significantly hence creating the least disturbing effects. Therefore, it is an alternate way to check the stability of the system when it is perturbed from the equilibrium. An analysis similar to previous velocity perturbation is carried out with different mound heights and perturbation strength as depicted in Table 3.5. But, with the same density perturbation strength, field lines are not significantly distorted. By $t = 5t_A$, the perturbation damps and settles into pockets of perturbed density which eventually weaken further and vanish at the boundaries by spreading. This is depicted in Figure 3.6.

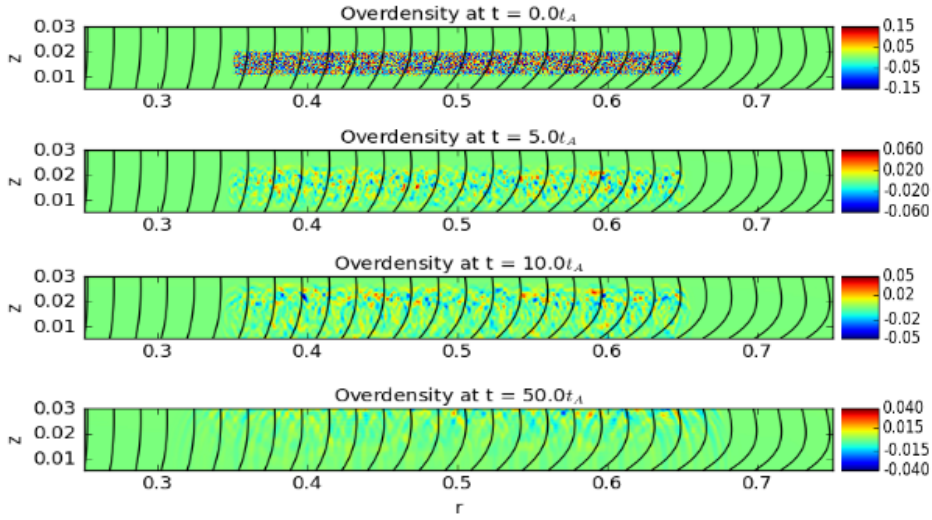


Figure 3.6: Over-density profiles of a mound with $Z_c = 45m$ and a zero mean density perturbation strength of 15% at different time steps

With increasing mound height (higher mass and pressure), it takes less time for the overdensity to dissipate by spreading out of the clumps of overdense regions faster.

In this 2D axisymmetric case, there is no signature of instabilities in the mounds of heights up to the threshold height ($\sim 72m$) for $B = 10^{12}G$. This is in agreement with Litwin et. al, 2001 [26] (LBR01, hereafter) which predicts the onset of interchange or ballooning modes to have finite toroidal wave vectors perpendicular to the local magnetic field, which requires a non-axisymmetric 3D system. It is crucial to model this system in 3D to capture the effect of toroidal instabilities [35]. In the next section, we intend to study the effect of non-zero mean density perturbations i.e. addition of excess mass to the accretion mound to understand gravity-driven instabilities.

Z_c (in meters)	Perturbation Strength	Max % error $t = 5t_A$	Max % error $t = 100t_A$
45	5	2.0	0.6
	10	3.2	1.6
	15	5.0	2.2
	20	7.5	2.75
	50	20.2	4.0
60	5	2.0	0.42
	10	3.0	0.7
	15	5.0	1.25
	20	6.75	2.0
	50	16.0	4.2
70	5	1.5	0.4
	10	2.5	0.5
	15	3.5	0.65
	20	5.0	1.1
	50	10.0	2.0

Table 3.5: Error in density due to zero mean density perturbation is shown at $t = 5t_A$ and $t = 100t_A$ in mounds of different heights while evolving the system through $100t_A$

3.5 Adding excess mass

To understand the dynamics of excess mass in the accretion mound, we add positive definite random number such that added matter is heavier than the environment and falls under gravity. Density in the perturbation zone is introduced as $\rho = \rho_0(1 + \eta\xi(r, z))$ such that $\langle \xi \rangle > 0$, without disturbing the pressure.

3.5.1 EOS

As extra mass is being added, it adds to the internal energy of the system which makes pressure independent of density as $p = \rho e(\gamma - 1)$ where e in the internal energy. This no longer keeps the energy equation redundant as in the barotropic case where $P = k_{ad}\rho^\gamma$. So, we use the Ideal EOS which solves the energy equation as well.

Upon adding positive density perturbation in barotropic EOS, a region of excess pressure is created which overcomes the effect of gravity acting downwards and pockets of added matter rise upwards. Hence, adiabatic EOS is required to study the

gravity-driven mode as it enables the matter to descend.

3.5.2 Boundary condition

Inner boundaries at the bottom and left are kept fixed ($Q = Q_0$) to their initial values. The bottom boundary is fixed as it is close to the crust which we assume to be solid [10]. The left boundary is close to the polar axis which has to be fixed from the symmetry point of view - if not, then matter will leak out from the centre in all direction leaving the centre empty. A fixed gradient condition is implemented at the outer boundaries at top and right where the initial gradients are preserved. This enables us to set the gradients of the perturbed quantities to zero ($\nabla Q = \nabla Q_0 + \nabla Q' \rightarrow \nabla Q_0, \nabla Q' = 0$)[34].

3.5.3 Inferences and Discussion

We run simulations with different values of positive definite density perturbation on mounds of different heights. Excess matter experiences a gravitational pull downward and a force sideways due to the lateral pressure gradient. This leads to the departure of the system from equilibrium.

There are two timescales involved: dynamical(t_{dyn}) and Alfvén(t_{Alf}). t_{dyn} is determined by the dominant acceleration due to gravity and t_{Alf} is related to the characteristics of the plasma.

$$t_{Alf} = L_0/v_{Alf} = 3.546 \times 10^{-4}s \quad (3.14)$$

$$t_{dyn} = \sqrt{L_0/g} = 0.232 \times 10^{-4}s \quad (3.15)$$

This shows that the dynamical timescales is shorter ($t_{dyn} = 0.065 t_{Alf}$) and hence dominates over the Alfvén timescale. So, the matter falls under the influence of gravity faster than spreading sideways. Figure 3.7 shows the predominantly downward acceleration at $t = 1t_A$. At $t = 0$, the pressure gradient in the z-direction(∇p_z) is more than that of the gradient in r-direction(∇p_r) as depicted by Equations 2.9 and 2.10 and their difference is plotted in Figure 3.8 which is balanced at equilibrium ($t = 0$). When additional density is introduced as a perturbation, ∇p_z increases further but

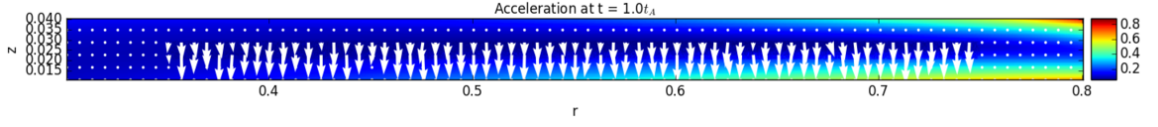


Figure 3.7: Normalised acceleration in the computational domain (scale shown in colorbar) and the direction of acceleration (shown by white arrows).

∇p_r does not change significantly due to no notable change in Ψ . Figure 3.9 highlights this difference persisting even at $t = 1t_A$ after perturbations are introduced.

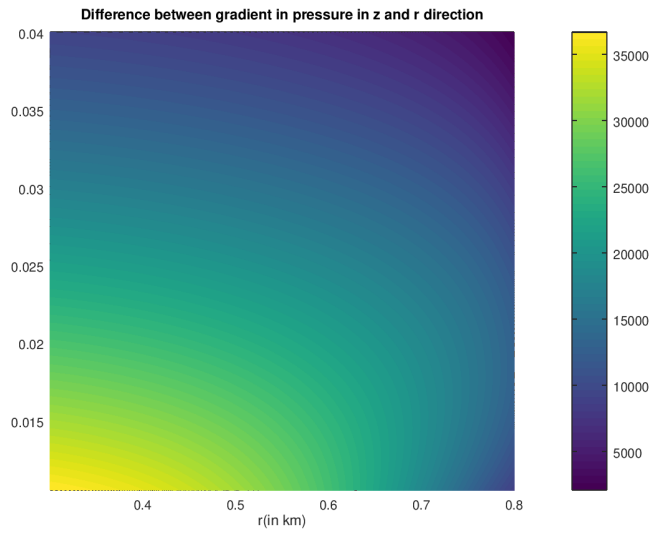


Figure 3.8: Difference between the pressure gradient in z and r direction is largely positive implying ∇p_z is more than ∇p_r by at least an order of magnitude

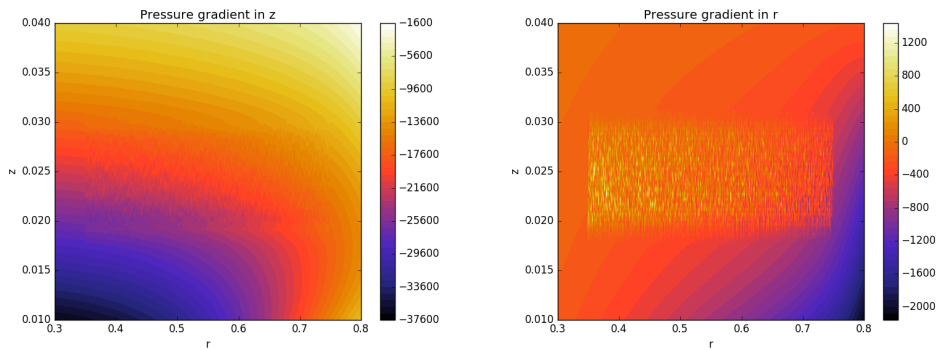


Figure 3.9: Pressure gradient upon introducing non-zero mean density perturbation along z (left) and r (right) at $t = 1t_A$ are shown here

η (in %)	Z_c (in m)		
	45	60	70
5	0.943	0.573	0.57
10	1.56	1.14	1.13
15	2.83	1.704	1.705
20	2.67	2.82	2.28
30	4.02	3.46	3.43
40	4.618	4.608	4.54
50	6.75	5.73	5.74

Table 3.6: Percentage of excess mass added to the mounds of different heights and density perturbation strength (η)

When less matter ($\eta < \eta_T$ i.e. threshold η) is added to the mound, it does not alter the mass of the region enough to get affected by gravity. The matter is supported by the lateral magnetic pressure and diffuses slightly into the surroundings. For high values of $\eta > \eta_T$, as the added matter descends it accumulates in some high-density pockets which distorts the equilibrium magnetic field topology and creates Parker instability type features. Temporal evolution of such features are shown in [Figure 3.10](#) and [Figure 3.11](#) for mounds of height 45m and 60m respectively. η_T for both the cases are discussed later in this section.

To quantify the distortion in the field lines for various perturbation strengths and mound heights, we measure the evolution of magnetic energy with time. Distortion implies higher tension ($\mathbf{B} \cdot \nabla \mathbf{B} / \mu_0$) in the field lines which is of the order B^2/L and hence proportional to the magnetic energy $B^2/8\pi$ for a given length scale in the mound. In [Figure 3.12](#), we have plotted the evolution of total magnetic energy normalised to its value at $t = 0$ for three different heights and for a various percentage of mass loading. The first plot for $Z_c = 45\text{m}$ shows a distinctive behaviour in the evolution trend beyond $\eta = 30\%$ of the existing mass in the computational domain. The magnetic energy starts increasing contrary to the decreasing trend for $\eta < 30\%$. This kind of bifurcation is a qualitative signature of the onset of gravity-driven instabilities. Similar behaviour is seen in the $Z_c = 60\text{m}$ mound for $\eta \sim 50\%$. In $Z_c = 70\text{m}$,

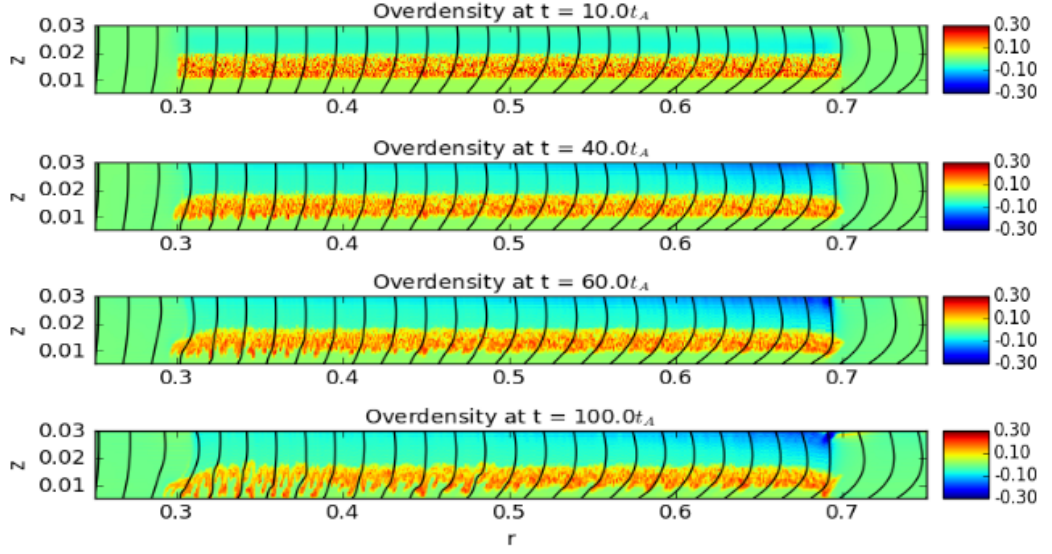


Figure 3.10: Over-density profiles of a mound with $Z_c = 45\text{m}$ and an excess mass of 4.02% ($\eta = 30\%$) at different time steps

for $\eta > 10\%$ similar trend in magnetic energy is observed due to closeness to the threshold height $Z_{max} = 72\text{m}$ for the dipolar magnetic field strength of 10^{12}G .

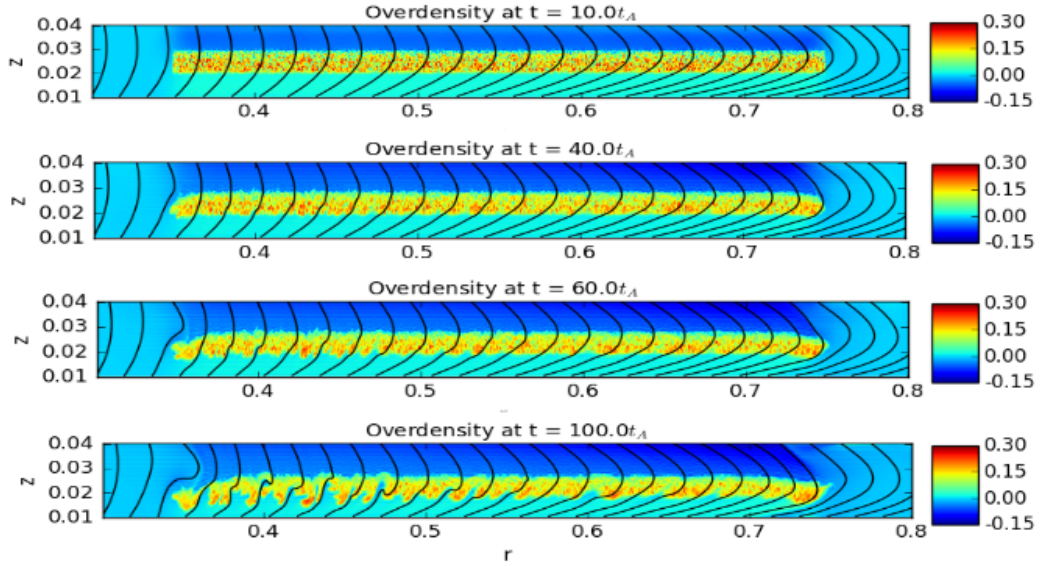


Figure 3.11: Over-density profiles of a mound with $Z_c = 60\text{m}$ and an excess mass of 3.46% ($\eta = 30\%$) at different time steps

We also investigate the kinetic energy evolution as shown in [Figure 3.13](#). Any distinct qualitative difference in its behaviour is not observed. But for $\eta > \eta_T$, the kinetic energy grows followed by a slower rate of growth which might lead to saturation at a time when the excess matter would settle down near the surface. Below this threshold, the kinetic energy asymptotes to a stable kinetic energy profile (note that the kinetic energy is zero at equilibrium). η_T reduces with height. For $Z_c = 45\text{m}$, $\eta_T \sim 30\%$ (4.02% excess mass); for $Z_c = 60\text{m}$, $\eta_T \sim 20\%$ (2.82% excess mass); for $Z_c = 70\text{m}$, $\eta_T \sim 10\%$ (1.13% excess mass).

But given that the maximum mass accretion rate (Eddington limit),

$$\dot{M}_{Edd} = 1 \times 10^{-3} M_{\odot} \text{ yr}^{-1} \frac{R_{star}}{R_{\odot}} \quad (3.16)$$

for a neutron star of radius 10km is $1.438 \times 10^{-8} M_{\odot} \text{ yr}^{-1}$ [1] and the mass of a stable mound is $\sim 10^{-12} M_{\odot}$, it is unlikely to encounter a physical situation where an excess mass in the order of $10^{-14} M_{\odot}$ is added over a timescale of seconds to initiate instabilities. Presence and intensity of gravity-driven instability in a real scenario have to be investigated further.

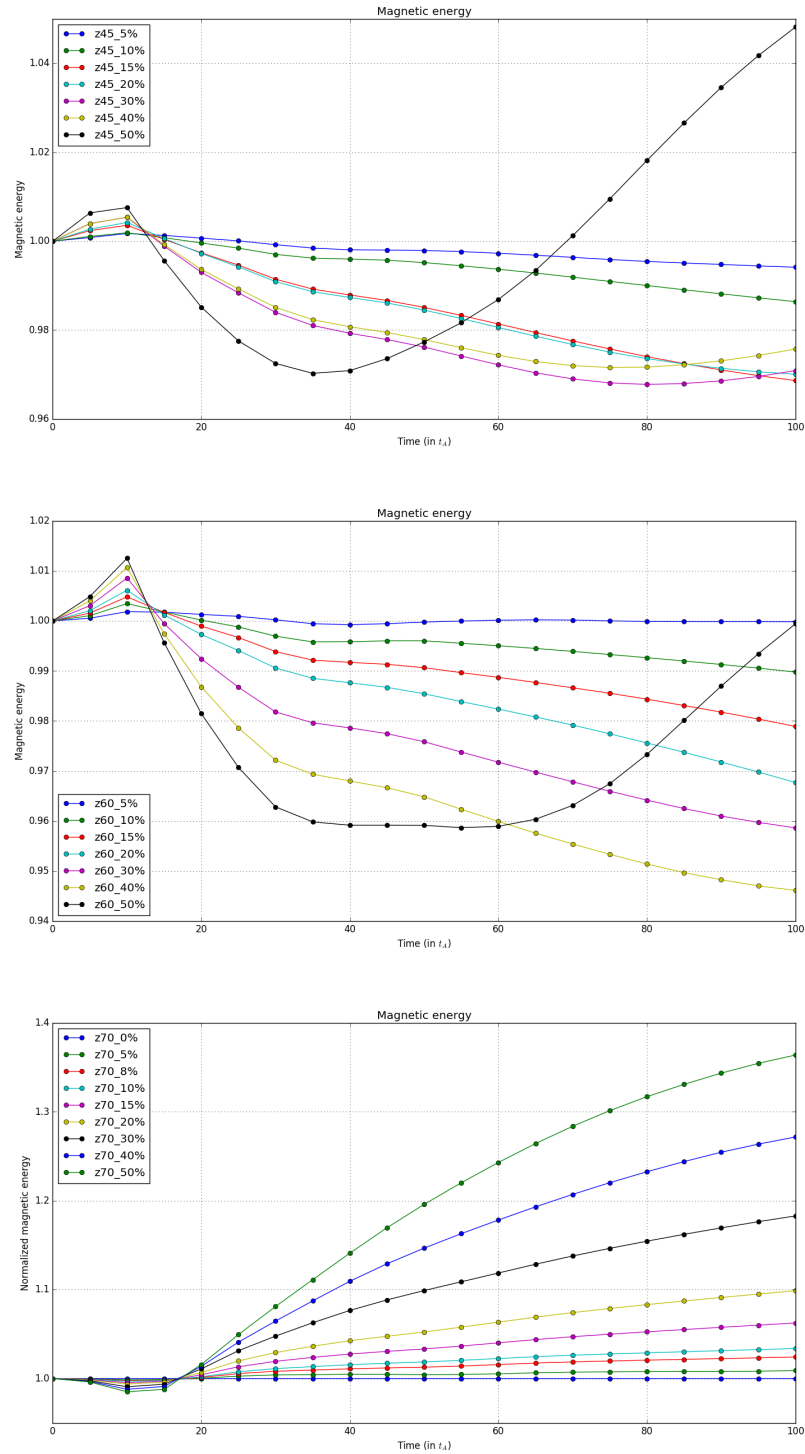


Figure 3.12: The figure shows the evolution of magnetic energy in mounds of height 45m (top), 60m (middle) and 70m (bottom) for a range of density perturbation strength from 5% to 50%

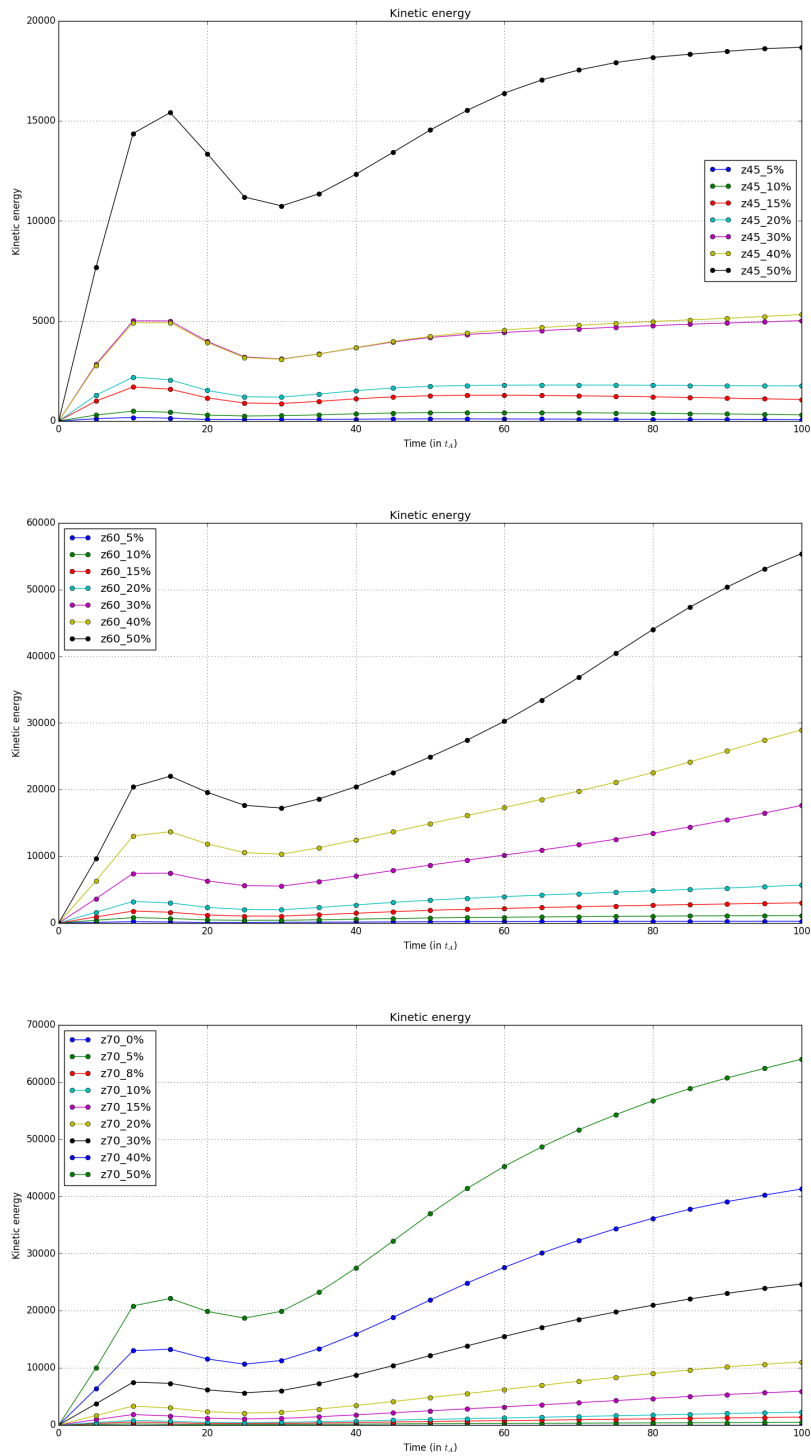


Figure 3.13: The figure shows the evolution of kinetic energy in mounds of height 45m (top), 60m (middle) and 70m (bottom) for a range of perturbation strength from 5% to 50%

Chapter 4

Polytropic vs Paczyński

With the similar setup in PLUTO as described for the non-relativistic degenerate Fermi EOS case ($P = k_{ad}\rho^\gamma$) (polytropic, hereafter), stability analysis of GS solution is carried out for mounds with Paczyński EOS, a general EOS that accounts for relativistic corrections. The expression for pressure in Paczyński EOS is given as

$$p = \frac{\pi m_e^4 c^5}{3 h^3} \frac{8/5 x_F^5}{(1 + 16/25 x_F^2)^{1/2}} \quad (4.1)$$

where x_F is the Fermi momentum as given in Eq. 2.27. The maximum error in overdensity in the computational domain turns out to be less than 1% implying our GS solution to be stable up to a maximum error threshold of 1%. We budget for this error while pursuing further dynamical studies.

In this chapter, we study the change in structure and magnetic field configuration of the mound when modelled by Paczyński EOS as compared to polytropic EOS. This will provide an idea about the offset in mound mass calculation when EOS is approximated to cover a non-relativistic degenerate regime.

4.1 Comparison on the basis of threshold height

The GS solution does not converge beyond a threshold height. This implies that the mound on a neutron star with a particular magnetic field can confine up to a

definite amount of matter while maintaining stability. The magnetic field lines cannot tolerate more tension and get distorted beyond this threshold. The threshold height for a polytropic and Paczyński mound is $\sim 72\text{m}$ and $\sim 56\text{m}$ respectively. Moreover, a Paczyński mound confines more matter than a corresponding polytropic mound of the same height. Because of the inclusion of relativity and in turn the softer equation of states ($P \propto \rho^{4/3}$), a Paczyński mound of any height can contain matter of density ($\geq 10^7 \text{g/cm}^3$). The threshold mass for Paczyński and non-relativistic case are around $11.08 \times 10^{-12} M_\odot$ (height $\sim 56\text{m}$) and $2.43 \times 10^{-12} M_\odot$ (height $\sim 72\text{m}$) respectively.

4.2 Comparison on the basis of mass

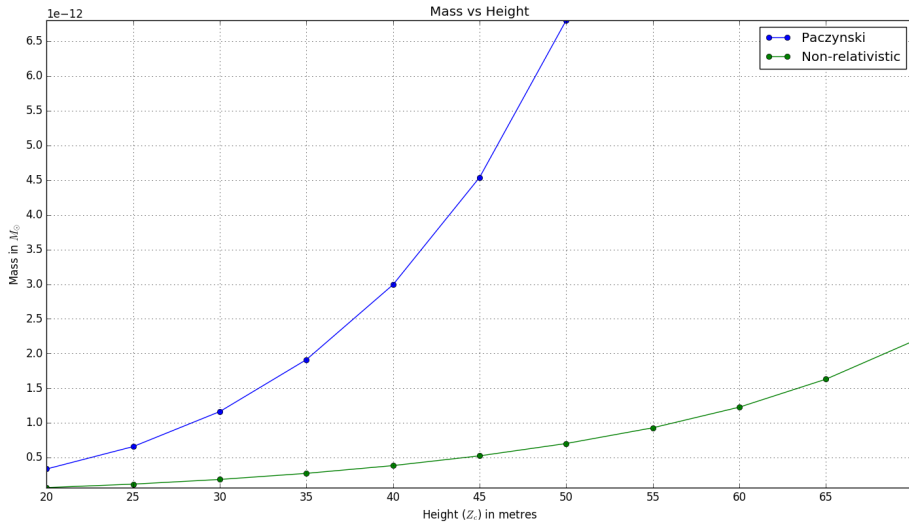


Figure 4.1: Comparison of confined mass in mounds of same height in Paczyński and Non-relativistic EOS.

We simulate mounds of different maximum central height for the polytropic and the Paczyński EOS, then we try to fit curves to find out a mathematical relation between mass and maximum central height (h) of mound. The dependence of total mound mass on the maximum central mound height can be approximated as $m \propto h^{2.72}$

for non-relativistic EOS and $m \propto h^{3.26}$ for Paczyński EOS. Paczyński mounds confine more mass for a given central mound height and magnetic field. Paczyński mounds manifest larger curvature and hence are more prone to interchange instabilities [35] at lower heights as compared to the polytropic mounds described in chapter 3.

4.3 Adding zero mean density perturbation

Paczyński EOS is a barotropic form of EOS i.e. $P = P(\rho)$. So, the qualitative behaviour of the density distribution after adding zero-mean density perturbation is similar to the non-relativistic degenerate polytropic EOS as mentioned in chapter 3. Table 4.1 shows the evolution of overdensity at $t = 5t_A$ and $t = 100t_A$ in Paczyński mounds of different heights. From the table, it can be inferred that the overdense regions spread out and become homogenous faster in comparison to a polytropic mound of the same central maximum height as mentioned in Table 3.5. This can be explained by the higher density (pressure) in the Paczyński mounds than polytropic mounds of comparable height. The initial overdensity is characterised by the density inside the mound and hence the maximum overdensity increases with mound height. But the dynamical parameters (velocity, acceleration due to gravity, lengthscale) determine the timescale for the spreading of perturbations. After evolving the system for $100t_A$ the maximum overdensity in a mound decreases with increase in height (and mass) as gravity influenced dynamical timescale dominates.

For a polytropic mound of height $Z_c = 45\text{m}$ (mass $\sim 1.04 \times 10^{-12} M_\odot$), the maximum error in density for perturbation strength 5%, 10%, 15% and 20% are 0.6%, 1.6%, 2.2% and 2.75% respectively which are greater than or equal to the error in case of a comparable Paczyński mound (in terms of mass) of height $Z_c = 25\text{m}$ (mass $\sim 1.30 \times 10^{-12} M_\odot$). So, Paczyński mounds reach steady-state almost at the same time or earlier than a polytropic mound of similar mass. This implies that the mass confined in the mound determines the timescale for the dynamics of the instabilities i.e. relaxation of perturbed pockets of matter as the mound is stable to the applied perturbations in $2D$.

Z_c (in meters)	Perturbation Strength	Max % error $t = 5t_A$	Max % error $t = 100t_A$
25	5	2.2	0.75
	10	4.2	1.4
	15	8.0	1.8
	20	6.8	2.7
30	5	2.0	0.5
	10	4.0	1.25
	15	7.0	1.75
	20	7.5	1.8
40	5	2.2	0.6
	10	4.5	1.0
	15	6.0	1.4
	20	8.0	2.8
50	5	2.5	0.4
	10	5.1	0.8
	15	6.2	0.85
	20	10.0	1.3

Table 4.1: Error in density due to zero mean density perturbation is shown at $t = 5t_A$ and $t = 100t_A$ in Paczyński mounds of different heights when the system is evolved through $100t_A$

4.4 Discussion

Using Paczyński EOS, we do not find any evidence of interchange instability as the mound settles down to a steady-state with an error of around 1% in density and velocity in $2D$. These simulations are sufficient to establish the difference in the structure and stability of the mounds under different EOS, especially highlighting the effect of inclusion of relativistic effects. Further instability analysis must be implemented using Paczyński EOS.

Chapter 5

Magnetohydrodynamic instabilities in the accretion mound

The stability of a plasma system determines the dynamics of the perturbations, whether they will grow or damp. Equilibrium is not permanent as perturbative forces are inevitable in a non-ideal dynamical system. These perturbations play an important role in energy conversion of modes and pose as the major hindrance for plasma confinement. Grad Shafranov solution is susceptible to instability upon introducing perturbations in the physical quantities like density and velocity. This puts a threshold on the maximum mound height and hence there exists a mass beyond which the mound becomes unstable. MHD instabilities limit the formation of large scale mounds as the GS solution becomes unstable under perturbations. In this chapter, we discuss the nature of such instabilities as investigated by studies like MB13a and MB13b.

5.1 Causes of instabilities

In this section, we discuss the possible origin of a few instabilities that have been explored previously and some of them are verified in this thesis as well for different equations of state.

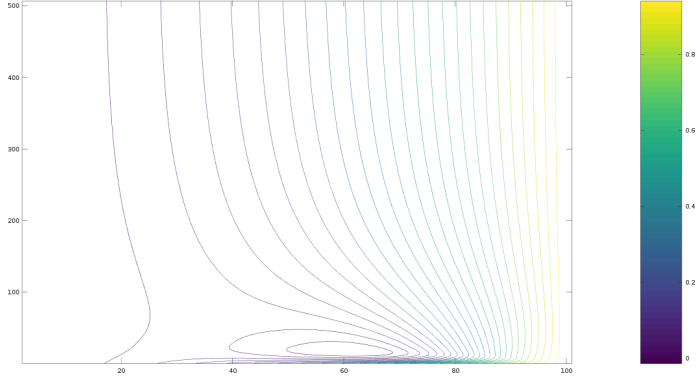


Figure 5.1: The magnetic flux profile for a mound of height $Z_c = 75\text{m}$ (higher than Z_{max}) at an intermediate time step as the solution does not converge. The axis labels show the number of grid points along that axis ranging upto 1km in x-axis and 0.1km in y-axis depicting r and z coordinates respectively. The colorbar shows the value of the magnetic flux contours.

Buoyancy related instabilities(Lack of numerical convergence)

Instability in GS solution is manifested in the form of closed loops in the magnetic flux profile when an iterative numerical scheme does not converge to a solution [19][38][34][35]. Closed field lines as shown in Figure 5.1 are not just some numerical discrepancy but are described as buoyant bubbles of plasma that rise from the surface of the neutron star and are inherently allowed in the solution domain by the model designed by PM04 and Vigelius and Melatos (2008)[46](VM08, hereafter). This happens when the tension in magnetic field lines ($\mathbf{B} \cdot \nabla \mathbf{B}$) can't balance plasma pressure gradients beyond a threshold mound height (mass). MB12 have proposed an analytical relation for determining the threshold height (Z_{max}) in terms of the normal magnetic field (B_n) and polar cap radius (R_p) beyond which the solution does not converge.

$$Z_{max} \propto B_n^{4/7} R_p^{2/7} \quad (5.1)$$

This result from the numerical study also agrees closely with the analytical stability criterion provided by LBR01 as

$$\log_{10}(Z_{max}) > -5.1 + (4/7) \log_{10} B \quad (5.2)$$

which sets a limit for the onset of pressure-driven ballooning instabilities.

Pressure-driven instabilities

The pressure-driven instability (interchange/ballooning instability) caused by gradients in magnetic pressure has been observed in confined plasma for example, in tokamak reactors. Brown and Bildsen (1998) [10] suggested that interchange instability could play a role in dragging magnetic field lines in accretion mounds equatorward and matter leaking out of the confinement. Analysis of such an instability is carried out by LBR01 for the plasma confined in the accretion mounds of a neutron star. As the name *interchange* suggests, this instability is created by an exchange of position of magnetic field line and plasma in the region where the confining magnetic field is curved. LBR01 investigated analytically the possibility of interchange modes in the accretion mound by using the energy principle. The energy integral of perturbed potential energy, δW is given as-

$$\delta W = \int \delta W(\Psi) d\Psi \quad (5.3)$$

where Ψ is the flux function used as a parameter and $\delta W(\Psi)$ is the potential energy per flux. By minimizing the energy integral, criteria for the onset of instability is found as:

$$\Delta\beta \geq 7.8R_p/h \quad (5.4)$$

Eq.5.4 ensures $\delta W(\Psi) < 0$ for some Ψ as it is a necessary and sufficient condition for instability.

The threshold mass required for the onset of instability is

$$\begin{aligned} \Delta M &\geq \pi R_p^2 (B^2/8\pi) (\Delta\beta/g) \\ &= 3.8 \times 10^{-13} M_\odot \left(\frac{B}{10^{12}G} \right)^2 \left(\frac{R_p}{1km} \right)^3 \left(\frac{Z}{26} \right)^{2/3} \left(\frac{A}{56} \right) \left(\frac{5 \times 10^8 K}{T} \right) \left(\frac{173}{\Gamma} \right) \end{aligned} \quad (5.5)$$

where $R_p \sim 10km$ is the radius of the polar cap, $h = c_s^2/g$ is the scale height, A is the atomic number, Γ is the Coulomb coupling constant.

This predicts interchange instability to grow even in mounds much less massive than the ones considered at magnetostatic equilibrium by Melatos & Phinney (2001)[28]

and PM04. When the instabilities manifest, there would be a loss of equilibrium and buoyant bubbles transport the magnetic flux upwards. Closed disconnected field lines are formed. This would limit the formation of large scale mounds as predicted by PM04.

MB13a test the stability of a magnetostatic accretion mound by using the MHD code PLUTO. They perform perturbation analysis numerically and report no interchange instability in a $2D$ axisymmetric mound. They highlight that the modes described by LBR01 are toroidal wave vectors and hence do not show up in $2D$. Although they do not see any sign of the instability, they find that the maximum β_{max} from their GS solution for a filled mound of certain height is greater than the threshold β_T evaluated from Eq.5.4 which calls for the onset of instability. It is also pointed out that the offset in plasma beta ($\beta_{max} - \beta_T$) increases with mound height, hence roughly implying that the instabilities grow faster with height (i.e. mass). This still keeps open the possibility of interchange instabilities in a higher dimension. So MB13b model the system in $3D$, introduce velocity perturbations to initiate interchange instability and establish the presence of interchange instability beyond a threshold mass. They numerically simulate the excitation of ballooning modes exhibited in the form of finger-like structures at the outer boundary of the mound, resulting in mass loss. In chapter 4, we have showed the consistency of the results of MB13a in $2D$ axisymmetric mound with a better EOS of Paczyński. We find no evidence of mass loss due to interchange instability in $2D$ and we observe that the system relaxes back to equilibrium with an error less than 1% when zero mean density and velocity perturbations are introduced.

Gravity-driven instabilities

In high mass mounds, MB13a [34] introduce excess mass as a perturbation to the equilibrium to investigate gravity-driven instabilities. This adds more pressure which in turn leads to the enhancement of the horizontal component of magnetic field making it prone to Parker instabilities due to higher curvature. These are the regions of high β where the matter is supported by tension from the field line curvature.

The energy integral derived from LBR01 for an adiabatic plasma is

$$\delta W = \frac{1}{2} \int d^3x \left\{ \frac{\tilde{B}_\perp^2}{4\pi} + \frac{B^2}{4\pi} (\nabla \cdot \xi_\perp + 2\kappa_c \cdot \xi_\perp)^2 + \gamma p (\nabla \cdot \xi - 2\kappa_g \cdot \xi)^2 - 2(\kappa_c + \nabla\phi/2c_s^2) \cdot \xi_\perp (\nabla p + \rho\nabla\phi) \cdot \xi_\perp \right\}$$

where ξ is the displacement, $\tilde{B} = \nabla \times (\xi \times \mathbf{B})$ is the perturbed magnetic field, $\kappa_c = (b \cdot \nabla)b$ is the magnetic field curvature vector, c_s is the sound speed and ϕ is the gravitational potential. As per the energy principle, instability sets in when $\delta W < 0$. MB13a and MB13b point out that if the terms containing field curvature, gravity and pressure gradient are negative enough, then they can exceed the magnetic pressure terms and render δW negative. This implies the presence of instabilities in the form of closed loops in mounds where the confining magnetic field lines have high curvature. MB13a induce such instability by adding positive density perturbation to the mound at equilibrium. When the perturbation strength(η) is low, matter settles down to a new equilibrium without disturbing the stability. When $\eta \geq \eta_T$ (threshold perturbation strength limited by the threshold β), the descending matter leads to bunching of field lines and reconnection leading to magnetic Rayleigh Taylor type (Parker) instabilities. The stretching of field lines converts internal and gravitational energy into magnetic energy and prevents the system from returning to a steady-state.

5.2 Discussion

From the previous studies, it can be concluded that the pressure-driven and the gravity-driven modes are responsible for the departure of the magnetostatic mounds from equilibrium beyond a certain threshold mound height(mass). They highlight the requirement of 3D modelling to capture the toroidal modes in interchange instability. In addition, they also managed to explain the mound stability up to a threshold height for a fixed magnetic field by showing the onset of gravity-driven instabilities due to the addition of excess mass. The works of Hameury et. al, 1983 [19], PM04 and VM08 establish the buoyancy related instabilities for the isothermal mounds. But these mounds do not represent the correct physical picture of accretion onto a neutron star. Nevertheless, the presence of buoyant topologically disconnected field lines is consistent with our numerical simulations based on the mound proposed by MB12.

Chapter 6

Summary

In this chapter, we present a summary of the work done in this thesis and propose future directions for the study.

6.1 Conclusions

- **Solving GS equation:** We solved the GS equation to understand the density and magnetic field structure of the accretion mounds for a non-relativistic degenerate Fermi (polytropic) EOS and Paczyński EOS (relativistic). We analyzed the relativistic effect on the matter confinement in the mound and concluded that a Paczyński mound can hold more matter as compared to a non-relativistic degenerate mound of the same height as a relativistic mound allows confinement of denser matter.
- **Checking stability:** We implemented the non-relativistic degenerate Fermi EOS and the relativistic Paczyński EOS in the MHD code PLUTO. Next, we performed 2D simulations to check the stability of our GS solution using PLUTO. After evolving the solution dynamically for $100t_A$, the error in density and velocity turned out to be an order of magnitude less than 1% and hence we concluded stability.
- **Looking for instabilities:** Taking into account the error from stability anal-

ysis, we introduced velocity and density perturbations in the mound. We analysed the dynamics of the perturbation with respect to the height of the mound. We found that the velocity and zero-mean density (no extra mass, just rearrangement of existing matter and field lines) perturbations relax to a steady-state faster with an increase in mound height(mass). We do not find pressure-driven interchange instabilities in our $2D$ simulations. $3D$ simulations as performed by MB13b must be carried out for better understanding of interchange instability. Next, we added excess mass to the mound. We observed magnetic Rayleigh Taylor type features for perturbation strength $\eta > \eta_T$ (threshold η determined by plasma β) for a particular maximum central mound height (Z_{max}). We find the results in agreement with MB13a. η_T and time of onset of such features decrease with Z_{max} .

- **Understanding MHD instabilities:** Analysing and understanding the MHD instabilities proposed by [26][34][35], we have tried to investigate those instabilities in a Paczyński mound. PM04, VM08 and MB13 helped in understanding the dynamical evolution of accretion mounds and gave an insight into the potential future work. Implementing the instability analysis to a mound modelled with Paczyński EOS leads to better representation of the problem.

6.2 Future Work

In the work done so far, a relation between the threshold mass(height) and distortion of the magnetic field in a stable mound has been established, beyond which the mound is de-stabilised [33]. The limitation is two-fold: the absence of continuous accretion(inflow) and mass loss out of confinement(outflow). Although MB13b confirmed the presence of instabilities, they have not addressed the spreading of matter out of the polar cap. The restrictive boundaries on the computational domain chosen inside the model (away from boundaries) limit the understanding of the dynamical evolution of the mound because of influx and outflux of matter at the system boundaries. Global magnetospheric accretion models [39] lack resolution to capture the flow of matter and distortion of field structures near the neutron star surface.

In order to describe a more realistic scenario that can be observed through cyclotron

lines, the inflow and outflow of matter need to be accounted for. This will give better estimates of mound size, density profile and magnetic field structure. This, in turn, will let us compare the simulated cyclotron lines with the observations and interpret the effect of accretion rate from the properties of these lines. The following are some improvements to be added -

- **Semi-relativistic setup to model leakage out of mound:** The interface between the mound and the neutron star atmosphere is required to be modelled to incorporate matter influx and spreading. The challenges ahead of us are - a numerical scheme to include two types of matter composition, handling Alfvén speeds close to the speed of light in low-density atmosphere and computational power to simulate the whole mound and the star atmosphere [22].
- **Non-uniform composition and thermal stratification:** In this thesis, we have considered the accretion mounds with uniform composition and temperature. But the infalling matter encounters a stratified density ($10^5 - 10^6 \text{g/cm}^3$) and pressure increasing towards the surface in the accretion column where the hydrogen and helium undergo nuclear reactions to get converted into carbon and higher elements [10]. As the matter descends and cools down, matter settles down in the form of a mound with a stratified chemical and thermal composition. Cumming et. al, 2001 [13] suggest buoyancy-driven instabilities due to the stratification in the mound beyond a threshold magnetic field ($10^{11} - 10^{12}$ G). They model this in a plane parallel geometry with a horizontal gradient in magnetic field which is an over-simplification. This is a significant loophole which misses out on the buoyancy related modes which must be included in modelling the spreading of matter out of the confinement in all directions. An EOS considering density as a function of matter composition and temperature needs to be implemented to model the stratification in the mound.
- **Interchange instabilities in 3D:** Instability in the interchange modes suggested by LBR01 is predominantly toroidal and has been numerically confirmed by MB13b. The corrections suggested above should be implemented in 3D for a self-consistent modelling of magnetic field configuration in the magnetically confined accretion mound taking into consideration the instabilities.

Appendices

Appendix A

Numerical setup to solve GS equation

We consider a grid with finer element in z-axis such that the distortions can be captured well. A PDE has unique solution if appropriate boundary conditions are specified. In a 2D space, the functional value (Ψ) or its normal derivative can be specified on the edge of the curve depending on what kind of boundary it is, in case of an elliptic PDE. The differential operators like the Grad-Shafranov operator are discretized.

$$\frac{\partial \Psi}{\partial x} \rightarrow \frac{\Psi_{i+1,j} - \Psi_{i-1,j}}{\Delta x^2} \quad (\text{A.1})$$

$$\frac{\partial^2 \Psi}{\partial x^2} \rightarrow \frac{\Psi_{i+1,j} - \Psi_{i,j} + \Psi_{i-1,j}}{\Delta x^2} \quad (\text{A.2})$$

By this method, discretized Grad-Shafranov equation becomes-

$$\Psi_{i,j} = \frac{\Psi_{i+1,j}(\frac{1}{\Delta r^2} - \frac{1}{2r\Delta r}) + \Psi_{i-1,j}(\frac{1}{\Delta r^2} + \frac{1}{2r\Delta r}) + \Psi_{i,j-1}(\frac{1}{\Delta z^2}) + \Psi_{i,j+1}(\frac{1}{\Delta z^2})}{Kr^2 + 2/\Delta r^2 + 2/\Delta z^2} \quad (\text{A.3})$$

where $K = \frac{2\rho g Z_c 4\pi r^2}{\Psi_p^2}$. An iterative method is used to solve this discretized equation.

It is a method in which a first approximation for the solution is constructed. It is used to obtain the second approximation which in turn is used to calculate the further approximations that leads to the correct solution.

$$\Psi_{i,j}^{(n+1)} = F(\Psi_{i-1,j-1}^n, \dots, \Psi_{i+1,j+1}^n) \quad (\text{A.4})$$

Here n represents the number of the iteration. This procedure tends to converge when the differences between the two successive iterations reaches a threshold value (tending to zero) as decided for the physical problem at hand.

A.1 Successive Over Relaxation

This method is better than both Jacobi and Gauss-Seidel as it uses some values of $\Psi_{i,j}$ from the updated step, not the previous approximation. Here is an example using a simple Laplacian equation with a source term $S_{i,j}$ and $\Delta x = h = \Delta y$, to show how the convergence is improved considerably using linear combination of old and new solutions.

$$\Psi_{i,j}^{n+1} = (1 - \omega)\Psi_{i,j}^n + \frac{\omega}{4}(\Psi_{i+1,j}^n + \Psi_{i-1,j}^{n+1} + \Psi_{i,j+1}^n + \Psi_{i,j-1}^{n+1} + h^2 S_{i,j}) \quad (\text{A.5})$$

In contrast, Gauss-Seidel method is as follows-

$$\Psi_{i,j}^{n+1} = (1 - \omega)\Psi_{i,j}^n + \frac{\omega}{4}(\Psi_{i+1,j}^n + \Psi_{i-1,j}^n + \Psi_{i,j+1}^n + \Psi_{i,j-1}^n + h^2 S_{i,j}) \quad (\text{A.6})$$

In case of Gauss-Seidel, $\omega = 1$. SOR method converges faster if $1 < \omega < 2$. Let r be the number of iterations required to to reduce the error by a factor of 10^{-p} , then -

$$\begin{aligned} r &= pN^2/4 \quad [\text{Gauss} - \text{Seidel}] \\ &= pN/3 \quad [\text{SOR}] \end{aligned} \quad (\text{A.7})$$

The generalized discretized PDE is formulated as follows-

$$a_{j,l}\Psi_{j+1,l} + b_{j,l}\Psi_{j-1,l} + c_{j,l}\Psi_{j,l+1} + d_{j,l}\Psi_{j,l-1} + e_{j,l}\Psi_{j,l} = f_{j,l} \quad (\text{A.8})$$

$$\Psi_{j,l}^{old} = \frac{1}{e_{j,l}} [f_{j,l} - a_{j,l}\Psi_{j+1,j} - b_{j,l}\Psi_{j-1,l} - c_{j,l}\Psi_{j,l+1} - d_{j,l}\Psi_{j,l-1}] \quad (\text{A.9})$$

$$\Psi_{j,l}^{new} = \Psi_{j,l}^{old} - \frac{resid}{e_{j,l}} \quad (\text{A.10})$$

where, $resid = a_{j,l}\Psi_{j+1,j} + b_{j,l}\Psi_{j-1,l} + c_{j,l}\Psi_{j,l+1} + d_{j,l}\Psi_{j,l-1} + e_{j,l}\Psi_{j,l} - f_{j,l}$

Appendix B

Equilibrium and stability in plasma confinement

This section is in reference to the book *Plasma Physics for Astrophysics* by Russell M. Kulsrud[24].

In an MHD system, motion is explained in terms of MHD waves. As magnetic field lines are frozen in plasma, these waves show the interplay between the motion \vec{v} and the magnetic field \vec{B} . Perturbations in $\{\rho, \vec{v}, p, \vec{B}\}$ are manifested in the form of waves about the equilibrium (smooth motion). When the scale of variation of perturbation becomes comparable to the scale of variation of equilibrium (or the undisturbed medium) the perturbations can grow and result into, either an oscillatory motion or an unstable motion. In an analogy to motion in a potential well in quantum mechanics, the negative and positive eigenfrequency modes corresponding to the bound and unbound state, give rise to oscillatory and unstable motion respectively. In order to understand the evolution of stability of a system, consider the following two cases. First, when there exists a static equilibrium in a rigid, insulating system with $\vec{v} = 0$, an instability can lead to conversion of potential energy (gravitational energy, pressure energy, magnetic energy etc) into kinetic energy. Increase in perturbation demands a growth in kinetic energy which is facilitated by the energy conversion. For example, a static atmosphere gets unstable when convection sets in due to perturbation, beyond a threshold temperature gradient. Second, in a non-static system ($\vec{v} \neq 0$), the already present kinetic energy is converted into other forms of kinetic energy. For example,

a rotating accretion disc becomes unstable to turbulent motion. Stability analysis enables us to study the growth of perturbations by varying some parameters specific to the system and predict the state of the equilibrium in time. So, given a system in static equilibrium we need to find parameters or constraints on normal modes which cause instability. There are two approaches to analyze stability -

- **Normal mode analysis** : According to this formulation, we need to check all modes to be sure about stability. If any one of the eigen modes is negative, the system becomes unstable. So, it is difficult to evaluate stability if all modes aren't examined. But it is useful in knowing the range of modes for which system is unstable unlike approaches which just give rise to a global instability.
- **Perturbed potential energy** : This method works by analyzing the perturbed potential energy. If the perturbed potential energy is negative, then the system is unstable. This method gives us information about global instability, not the specific range of modes. For example, in the calculation of Jeans stability mass, if we calculate by this method it just tells that the system will collapse but not the range of wavelength/modes where it will collapse. So, the normal mode method works better in this example.

B.1 Energy Principle

Consider static equilibrium where $\{\rho, \vec{j}, p, \vec{B}\} = \{\rho_0(r_0), \vec{j}_0(r_0), p_0(r_0), \vec{B}_0(r_0)\}$ are functions of position at equilibrium and independent of time. The system is assumed to be bound by a rigid wall and magnetic field is tangent to the surface, to ensure conservation of energy in the volume of interest. At $t = 0$, perturbation is introduced in initial position and velocity. Applying the action principle for MHD, equations for the perturbed physical quantities $\rho(t, \vec{r}), \vec{j}(t, \vec{r}), p(t, \vec{r})$ and $\vec{B}(t, \vec{r})$ are obtained. Using these perturbed quantities, the perturbed Euler equation is calculated which is essentially the equation of motion for the perturbation at $t > 0$.

$$\rho_0 \frac{\partial^2 \vec{\zeta}}{\partial t^2} = \vec{F}(\vec{\zeta}) \quad (\text{B.1})$$

where $\vec{F}(\vec{\zeta})$ describes first order in $\vec{\zeta}$, the force per unit volume on each fluid particle induced by the perturbation that accelerates the plasma. Energy(ε) is conserved for any arbitrary displacement to all orders of magnitude. Consider accuracy till second order for further calculations. So, we can write W by decomposing it into terms with different order contributions in $\vec{\zeta}$. $W = W_0 + W_1(\vec{\zeta}) + W_2(\vec{\zeta}, \vec{\zeta})$, where W_0 is the unperturbed value and W_1 and W_2 describe the potential energy density first order and second order in $\vec{\zeta}$ respectively.

$$\varepsilon = \frac{1}{2} \int \rho_0(\vec{r}) \left(\frac{\partial \vec{\zeta}}{\partial t} \right)^2 dV + W(\vec{\zeta}, \vec{\zeta}) \quad (\text{B.2})$$

Functional W is quadratic in $\vec{\zeta}$ and depicts the change in potential energy due to perturbation. We look at normal mode solutions in the form $\zeta = \hat{\zeta} e^{i\omega t}$ for the perturbed Euler equation. Substituting the normal mode solution and considering the force equation and its complex conjugate, followed by some algebra gives some important results. If $\omega^2 > 0$, then ω is real and the normal mode is stable. Otherwise when $\omega^2 < 0$, $\omega = i\lambda$ gives solutions that either purely grow for $\lambda > 0$ or damp for $\lambda < 0$. This implies that a mode can't grow and oscillate at the same time. Now we define a parameter Λ to track each normal mode as it transitions from stability to instability.

$$\Lambda = \frac{W_2(\vec{\zeta}, \vec{\zeta})}{K(\vec{\zeta}, \vec{\zeta})} \quad (\text{B.3})$$

where

$$K = \int \rho_0(\vec{\zeta})^2 dV \quad W_2 = - \int \rho_0(\vec{\zeta}) \cdot \vec{F}(\vec{\zeta}) dV \quad (\text{B.4})$$

Using the expansion $\vec{\zeta} = \sum a_n \vec{\zeta}_n$ as superposition of all modes and simplifying, we find

$$\Lambda = \frac{\sum \omega_n^2 a_n^2}{\sum a_n^2} \geq \omega_1^2. \quad (\text{B.5})$$

If $\Lambda > 0$ for all modes ($\vec{\zeta}$), then the system is stable. Conversely, if $\Lambda < 0$ for any normal mode then the whole system is unstable. As K being the mean squared perturbed energy is always positive, a necessary and sufficient condition for stability is that the change in perturbed potential energy W_2 is positive for all modes. This is the MHD energy principle. Furthermore, the perturbed potential energy integral

can be minimized to obtain a better bound on the parameter tracing stability. It isn't straightforward to apply Energy principle to systems in non-static equilibrium where a flow is present. By simply lowering the potential energy ($\delta W < 0$), it can't be expected to introduce instability.

Bibliography

- [1] Eddington rate calculation. <https://jila.colorado.edu/~pja/astr3730/lecture18.pdf>.
- [2] Bachetti, M., Romanova, M. M., Kulkarni, A., Burderi, L., and di Salvo, T. (2010). QPO emission from moving hot spots on the surface of neutron stars: a model. *Monthly Notices of the Royal Astronomical Society*, 403(3):1193–1205.
- [3] Backer, D., K. S. and Heiles, C. (1982). A millisecond pulsar. *Nature*, 300:615–618.
- [4] Balsara, D. S. and Spicer, D. S. (1999). A staggered mesh algorithm using high order godunov fluxes to ensure solenoidal magnetic fields in magnetohydrodynamic simulations. *Journal of Computational Physics*, 149(2):270 – 292.
- [5] Balsara, S. D. *The Hydrodynamical Riemann Problem*, chapter 5.
- [6] Becker, P. A. and Wolff, M. T. (2007). Thermal and Bulk Comptonization in Accretion-powered X-Ray Pulsars. *The Astrophysical Journal*, 654(1):435–457.
- [7] Bhattacharya, D. and van den Heuvel, E. (1991). Formation and evolution of binary and millisecond radio pulsars. *Physics Reports*, 203(1):1 – 124.
- [8] Bisnovatyi-Kogan, G. S. and Komberg, B. V. (1974). Pulsars and close binary systems. *Soviet Astronomy*, 18:217.
- [9] Braithwaite, J. and Spruit, H. C. (2006). Evolution of the magnetic field in magnetars. *Astronomy and Astrophysics*, 450(3):1097–1106.
- [10] Brown, E. F. and Bildsten, L. (1998). The Ocean and Crust of a Rapidly Accreting Neutron Star: Implications for Magnetic Field Evolution and Thermonuclear Flashes. *The Astrophysical Journal*, 496(2):915–933.

- [11] Chamel, N. and Haensel, P. (2008). Physics of Neutron Star Crusts. *Living Reviews of Relativity*.
- [12] Coburn, W. (2001). *A study of magnetic fields of accreting X-ray pulsars with the Rossi X-ray Timing Explorer*. PhD thesis, UNIVERSITY OF CALIFORNIA, SAN DIEGO.
- [13] Cumming, A., Zweibel, E., and Bildsten, L. (2001). Magnetic screening in accreting neutron stars. *The Astrophysical Journal*, 557.
- [14] Fabbiano, G. and Schreier, E. J. (1977). Further studies of the pulsation period and orbital elements of Centaurus X-3. *The Astrophysical Journal*, 214:235–244.
- [15] Farouki, R. T. and Hamaguchi, S. (1993). Thermal energy of the crystalline one-component plasma from dynamical simulations. *Physics Rev. E*, 47(6):4330–4336.
- [16] Ghosh, P. and Lamb, F. K. (1979). Accretion by rotating magnetic neutron stars. II. Radial and vertical structure of the transition zone in disk accretion. *The Astrophysical Journal*, 232:259–276.
- [17] Ghosh, P., Lamb, F. K., and Pethick, C. J. (1977). Accretion by rotating magnetic neutron stars. I. Flow of matter inside the magnetosphere and its implications for spin-up and spin-down of the star. *The Astrophysical Journal*, 217:578–596.
- [18] Gold, T. (1969). Rotating Neutron Stars and the Nature of Pulsars. *Nature*.
- [19] Hameury, J. M., Bonazzola, S., Heyvaerts, J., and Lasota, J. P. (1983). Magnetohydrostatics in the polar caps of the gamma-ray burst sources. *Astronomy and Astrophysics*, 128(2):369–374.
- [20] Hulse, R. A. and Taylor, J. H. (1975). Discovery of a pulsar in a binary system. *The Astrophysical Journal*, 195:L51–L53.
- [21] Jaranowski, P., K. A. and Schutz, B. F. (1998). The binary pulsar: physical processes, possible companions, and evolutionary histories. *Physics Review D*, 58.
- [22] Konar, S. and Choudhuri, A. R. (2004). Diamagnetic screening of the magnetic field in accreting neutron stars — II. The effect of polar cap widening. *Monthly Notices of the Royal Astronomical Society*, 348(2):661–668.

-
- [23] Kulkarni, A. K. and Romanova, M. M. (2008). Accretion to magnetized stars through the Rayleigh–Taylor instability: global 3D simulations. *Monthly Notices of the Royal Astronomical Society*, 386(2):673–687.
- [24] Kulsrud, R. M. *Plasma Physics for Astrophysics*, chapter Plasma Instabilities. Princeton U. Press, Princeton, NJ.
- [25] Lamb, F. K., Pines, D., and Shaham, J. (1976). *Information about accretion flows from X-ray timing of pulsating sources.*, volume 389, pages 141–153. NASA Special Publication.
- [26] Litwin, C., Brown, E., and Rosner, R. (2001). Ballooning instability in polar caps of accreting neutron stars. *The Astrophysical Journal*, 533:788–795.
- [27] Long, M., R. M. M. and Lovelace, R. V. E. (2008). Three-dimensional simulations of accretion to stars with complex magnetic fields. *Monthly Notices of the Royal Astronomical Society*, 386(3):1274–1284.
- [28] Melatos, A. and Phinney, E. S. (2001). Hydromagnetic Structure of a Neutron Star Accreting at Its Polar Caps. *Publications of the Astronomical Society of Australia*, 18(4):421–430.
- [29] Mignone, A. (2007). A simple and accurate riemann solver for isothermal mhd. *Journal of Computational Physics*, 225(2):1427 – 1441.
- [30] Mignone, A., Bodo, G., Massaglia, S., Matsakos, T., Tesileanu, O., Zanni, C., and Ferrari, A. (2007). PLUTO: A numerical code for computational astrophysics. *The Astrophysical Journal Supplement Series*, 170(1):228–242.
- [31] Mukherjee, D. (2014). *Probing the evolution of the magnetic field of accreting neutron star binaries*. PhD thesis, Inter-university centre for astronomy and astrophysics, Jawaharlal Nehru University, New Delhi.
- [32] Mukherjee, D. (2017). Revisiting Field Burial by Accretion onto Neutron Stars. *Journal of Astrophysics and Astronomy*, 38.
- [33] Mukherjee, D. and Bhattacharya, D. (2012). A phase-dependent view of cyclotron lines from model accretion mounds on neutron stars. *Monthly Notices of the Royal Astronomical Society*, 420(1):720–731.

- [34] Mukherjee, D., Bhattacharya, D., and Mignone, A. (2013a). MHD instabilities in accretion mounds – I. 2D axisymmetric simulations. *Monthly Notices of the Royal Astronomical Society*, 430(3):1976–1987.
- [35] Mukherjee, D., Bhattacharya, D., and Mignone, A. (2013b). MHD instabilities in accretion mounds – II. 3D simulations. *Monthly Notices of the Royal Astronomical Society*, 435(1):718–727.
- [36] Pacini, F. (1967). Energy Emission from a Neutron Star. *Nature*.
- [37] Paczynski, B. (1983). Models of X-ray bursters with radius expansion. *The Astrophysical Journal*, 267:315–321.
- [38] Payne, D. J. B. and Melatos, A. (2004). Burial of the polar magnetic field of an accreting neutron star - I. Self-consistent analytic and numerical equilibria. *Monthly Notices of the Royal Astronomical Society*, 351(2):569–584.
- [39] Romanova, M., Long, M., Kulkarni, A., Kurosawa, R., Ustyugova, G., Koldoba, A., and Lovelace, R. (2008). Mhd simulations of disk-star interaction. *Proceedings of the International Astronomical Union*, 3.
- [40] Rothschild, R., Staubert, R., Wilms, J., Santangelo, A., Kretschmar, P., Kreykenbohm, I., Pottschmidt, K., Schönherr, G., McBride, V., Kendziorra, E., Shakura, N., Postnov, K., Klochkov, D., Nishimura, O., Wilson-Hodge, C., Wolff, M., and Wood, K. (2020). Decadal review white paper physics of the accretion mound at the magnetic poles of neutron stars.
- [41] Shapiro, S. L. and Teukolsky, S. A. (2007). *Neutron Star Models: Masses and Radii*, chapter 9, pages 241–266. John Wiley & Sons, Ltd.
- [42] Smarr, L. L. and Blandford, R. (1976). The binary pulsar: physical processes, possible companions, and evolutionary histories. *The Astrophysical Journal*, 207:574–588.
- [43] Smartt, S. J. (2009). Progenitors of core-collapse supernovae. *Annual Review of Astronomy and Astrophysics*, 47(1):63–106.
- [44] Srinivasan, G. and van den Heuvel, E. P. J. (1982). Some constraints on the

- evolutionary history of the binary pulsar PSR1913+16. *Astronomy & Astrophysics*, 108:143–147.
- [45] Toro, E. F. (2008). *Riemann Solvers and Numerical Methods for Fluid Dynamics*. Springer, Berlin.
- [46] Vigelius, M. and Melatos, A. (2008). Three-dimensional stability of magnetically confined mountains on accreting neutron stars. *Monthly Notices of the Royal Astronomical Society*, 386(3):1294–1308.
- [47] Wijnands, R. and van der Klis, M. (1998). A millisecond pulsar in an X-ray binary system. *Nature*, 394(6691):344–346.
- [48] Yakovlev, D. G., Haensel, P., Baym, G., and Pethick, C. (2013). Lev Landau and the concept of neutron stars. *Physics-Uspekhi*, 56(3):289–295.